CHALMERS
UNIVERSITY OF TECHNOLOGY

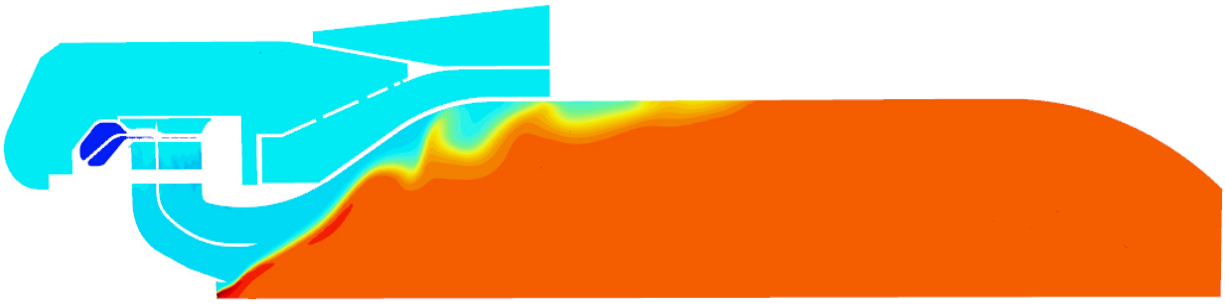

Performance of Cracked Ammonia Combustion in a Gas Turbine Engine

Evaluation through CFD and chemical reactor network modeling

Master's thesis in Sustainable Energy Systems

JOHANNA LINDFORS

DEPARTMENT OF MECHANICHS AND MARITIME SCIENCES

Chalmers University of Technology
Gothenburg, Sweden 2022
www.chalmers.se

Master's thesis 2022

Performance of Cracked Ammonia Combustion in a Gas Turbine Engine

Evaluation through CFD and chemical reactor network modeling

JOHANNA LINDFORS

CHALMERS
UNIVERSITY OF TECHNOLOGY

Department of Mechanics and Maritime Sciences
Division of fluid dynamics
Chalmers University of Technology
Gothenburg, Sweden 2022

Performance of Cracked Ammonia Combustion in a Gas Turbine Engine
Evaluation through CFD and chemical reactor network modeling
JOHANNA LINDFORS

Supervisor: Karl-Johan Nogenmyr, Siemens Energy AB
Examiner: Tomas Grönstedt, Department of mechanics and maritime sciences

Master's Thesis 2022
Department of Mechanics and Maritime Sciences
Division of fluid dynamics
Chalmers University of Technology
SE-412 96 Gothenburg
Telephone +46 31 772 1000

Cover: CFD simulation of a cracked ammonia flame in the combustor sector model

Typeset in LaTeX
Printed by Chalmers Reproservice
Gothenburg, Sweden 2022

Performance of Cracked Ammonia Combustion in a Gas Turbine Engine
Evaluation through CFD and chemical reactor JOHANNA LINDFORS
Department of Mechanics and Maritime Sciences
Chalmers University of Technology

Abstract

The issue of global warming and the increasing global energy demand requires introduction of new, renewable fuels for energy- and electricity production. If generated from green hydrogen, ammonia could be of particular importance in future sustainable energy systems as an energy carrier and a carbon free gas turbine fuel. Opposed to hydrogen, transportation and storage of ammonia is already widely established and easily facilitated; however, the combustion properties of pure ammonia are not feasible with a turbulent gas turbine environment due to low reactivity. By partially cracking ammonia into its elementary components, suitable combustion properties can be obtained. Ammonia combustion is also prone to substantial levels of NO_X and N_2O emissions. However, adoption of rich-lean staging has previously been shown to mitigate NO_X emissions from the combustion process. In this thesis, the combustion performance of cracked ammonia in the SGT-750 gas turbine combustor, provided by Siemens Energy AB, is evaluated in terms of emissions and flame stability. Numerical CFD and chemical reactor network (CRN) models are used to investigate the feasibility of different fuel compositions, originating from cracked ammonia, as gas turbine fuels. Equivalence ratios ranging from approximately 0.4 to 1.5 are investigated, in single stage and air-staged combustion. The results revealed that flame stability was achievable for ammonia cracking degrees of at least 40% at lean conditions, and NO_X emissions below 100 ppmvd were emitted for rich-lean staged combustion. Global warming potentials, as CO_2-equivalents, far below those of conventional natural gas combustion were found for several fuel compositions and equivalence ratios. However, great discrepancies were apparent among the resulting N_2O emissions from the different models. Thus, further experimental validation of the applied computational models and chemical mechanism is required, to establish the environmental performance of cracked ammonia as a gas turbine fuel.

Keywords: CFD, CRN, ammonia, hydrogen, gas turbines, combustion, NO_X, N_2O

Acknowledgements

I would like to thank the employees at Siemens Energy AB for the opportunity to perform this master thesis project at the R&D department in Finspång, for your extensive knowledge and eagerness to help. I would particularly like to express my gratitude towards my supervisor at Siemens Energy AB, Karl-Johan Nogenmyr, for your extensive support and knowledge, for your engagement and our inspirational discussions. My deepest appreciations also go to my examiner, Tomas Grönstedt, professor at the department of mechanics and maritime sciences, division of fluid dynamics, for your valuable feedback on this master thesis project.

Johanna Lindfors, Gothenburg, June 2022

List of Acronyms

Below the acronyms that have been used throughout this thesis are listed in alphabetical order:

AFT	Adiabatic Flame Temperature
CCM	Complex Chemistry Model
CD	Cracking Degree
CFD	Computational Fluid Dynamics
CFL	Courant-Friedrichs-Lewy
CRN	Chemical Reactor Network
Da	Damköhler number
EB	Elliptic-Blending
EDC	Eddy Dissipation Concept
ER	Equivalence Ratio
FGM	Flamelet Generated Manifold
GT	Gas Turbine
ISAT	In-Situ Adaptive Tabulation
Ka	Karlovitz number
Le	Lewis number
LFC	Laminar Flame Concept
PFR	Plug Flow Reactor
PSR	Perfectly Stirred Reactor
RANS	Reynolds-Averaged Navier-Stokes
Re	Reynolds number
RPL	Rich Pilot Lean
RST	Reacting Species Transport
RSTT	Reynolds Stress Transport Turbulence
SCR	Selective Catalytic Reduction
TFSC	Turbulent Flame Speed Closure
URANS	Unsteady Reynolds-Averaged Navier-Stokes

Nomenclature

Below is the nomenclature of indices, parameters, and variables that have been used throughout this thesis.

Indices

i, j, k	Dummy indices for variable or species
gen	Generation
PZ	Primary zone
st	Stoichiometric conditions
SZ	Secondary zone
t	Index for turbulent variable

Parameters

C_μ, C_T. C_t	$k-\varepsilon$ turbulence model constants
$C_{\varepsilon 1}$, $C^*_{\varepsilon 2}$	Lag-EB turbulence model constants
C_{l1}, C_{l2}	Complex chemistry model constants
D_f	Turbulent diffusivity
$\bar{E}$	Mean energy
$\dot{m}$	Mass flow
k	Turbulent kinetic energy
L	Large-eddy length scale/Turbulent length scale
p	Pressure
ϕ_{PZ}	Primary zone equivalence ratio
ϕ_{SZ}	Secondary zone equivalence ratio
R	Universal gas constant, 8.3145 $J/(mol \cdot K)$
r_k	Reaction rate of species k
s_L	Laminar flame velocity

S_i	Source term of variable i
$\mathbf{S}$	Strain rate tensor
T	Temperature
T_{ad}	Adiabatic flame temperature
t	Time
t_t	Turbulent time scale
$\bar{\mathbf{T}}$	Mean viscous stress tensor
$\mathbf{T_{RANS}}$	Turbulent stress tensor
u	Local velocity
$\bar{\mathbf{U}}$	Mean convective velocity
V	Volume
Y	Species mass fraction
Z	Mixture fraction

Greek letters

α	Elliptic blending factor
η	Kolmogorov length scale
$\eta_{comb,tot}$	Total combustion efficiency
ε	Turbulent dissipation rate
μ	Dynamic viscosity
μ_t	Turbulent dynamic viscosity
ν	Kinematic viscosity
$\dot{\omega}$	Species production rate
ρ	Density
φ	Wall-normal stress component
ϕ	Equivalence ratio
ψ	Arbitrary quantity of the flow
τ_η	Kolmogorov time scale
σ_ε, σ_k, σ_ϕ	Lag-EB turbulence model constants

Contents

1

Introduction

1.1 Background

The issue of global warming demands a shift from fossil-based to renewable energy sources. Along with an increasing electricity demand globally, the search for renewable energy sources is of particular importance to the electricity sector. Ammonia generated from green hydrogen and nitrogen has the potential of constituting a renewable energy carrier with zero carbon comprised greenhouse gas emissions [1]. The fuel could also provide balance in a renewable-based electricity system during seasons of non-favourable climate [2]. Thanks to the long history of ammonia production, distribution- and storage systems are already widely established, which is not the case for other renewable fuels such as hydrogen [3]. Pure ammonia does unfortunately not possess the combustion properties required for extensive use in present gas turbine designs due to its low reactivity, flame speed and narrow flammability limits [1, 4]. However, by cracking ammonia into its elementary components, H_2 and N_2, before combustion, a fuel mix with more suitable combustion properties can be generated.

With steam and nitrogen gas being the only primary products, combustion of ammonia and hydrogen generates neither carbon dioxide nor carbon monoxide. Unfortunately, large amounts of nitrous oxide, N_2O, and nitrogen oxides, NO and NO_2 (NO_X), can be formed in the process [1, 5]. The formation of NO_X in combustion of ammonia differs from that of conventional hydrocarbon combustion, in that the fuel itself constitutes a source of nitrogen. Hence, the mechanism behind NO_X mitigation is somewhat different in NH_3/H_2 combustion compared to that of carbon fuels. Furthermore, little is still known about flame stability of ammonia/hydrogen fuels [6]. Flame stability is crucial to combustion in gas turbines, to enable steady-state operation and to avoid unnecessary damage of the equipment.

If successfully stabilising ammonia flames and mitigating NO_X and N_2O emissions, ammonia could play an important role in the energy system as a fully renewable gas turbine fuel. Exchanging conventional hydrocarbon fuels for non-carbon based gas mixtures with similar combustion properties could also enable retrofitting of existing combustion processes, which is attractive from an economic point of view [4]. This is also true for Siemens Energy AB, who would benefit largely from being able to switch to renewable fuels while keeping already existing gas turbine designs. Therefore, the primary objective of this master thesis project is to evaluate flame stability

and emission levels of different ammonia/hydrogen fuel mixes, in the combustor of the gas turbine model SGT-750.

1.1.0.1 Previous work at Siemens Energy

Several mesh optimization and model stability studies were performed on the SGT-750 sector model used in this project. M. Safari compared the residual stability obtained for two different turbulence models; the Lag EB k-ε and the SST k-ω model [7]. The Lag EB k-ε model was concluded to improve stability for the residuals and monitored properties such as velocity, equivalence ratio and mass flow in the first main channel. S. Reinberth performed a mesh independence study on the same model, to reduce the number of cells and make simulations more efficient [8]. The distribution of equivalence ratio and velocity magnitude in the first main channel were used as parameters for evaluation of mesh dependency. He introduced mesh refinements at the fuel jets, which was shown to improve convergence. The same parameters were used by W. Charoenchang, who used a jet-in-crossflow model to test different mesh strategies for the main jets and channels [9]. Mesh refinements surrounding the jets, geometrically formed as cylinders, were implemented. Due to the accomplished improvements, the mesh will not be further optimized in this project.

1.1.1 Aim

The aim of this thesis is to perform primary analysis on the potential of partially cracked ammonia as a fuel for the SGT-750 gas turbine model, provided by Siemens Energy AB. The analysis will be performed with respect to flame stability and emissions of NO_X and N_2O. Fuel configuration that exhibit stable flame properties and show reasonable emissions levels will be identified for further, detailed analysis at Siemens Energy AB. Combustion of different $NH_3/H_2/N_2$ fuel mixes will be simulated with CFD through the software STAR-CCM+, as well as chemical reactor network modeling using the python-integrated package Cantera. The ammonia dissociation degree will range from zero to one, and several equivalence ratios will be investigated.

1.1.2 Limitations

The simulations performed in this project will cover only the 30° SGT-750 burner section. Hence the flow field in the compressor and turbine, upstream and downstream of the combustor respectively, will not be included in the computational models. This project will not look into the detailed flow patterns occurring in the combustion chamber, including possible effects of local mixing on the flow and combustion products. Neither will the process requirements of ammonia cracking, or any economical aspects thereof, be examined.

1.2 Gas turbine SGT-750

The SGT-750 gas turbine model, provided by Siemens Energy AB, is designed for industrial applications and has a simple cycle gross power output of 39.8 MW_e [10]. The gas turbine consists of a 13-stage axial air compressor, 8 combustion vessels and a two-stage axial power turbine. The full design is shown in Figure 1.1, where the compressor and turbine are colored blue and orange, respectively. The SGT-750 operates with either gaseous or liquid fuels. The present burner design is also compatible with hydrogen-containing fuels, up to 40% hydrogen content.

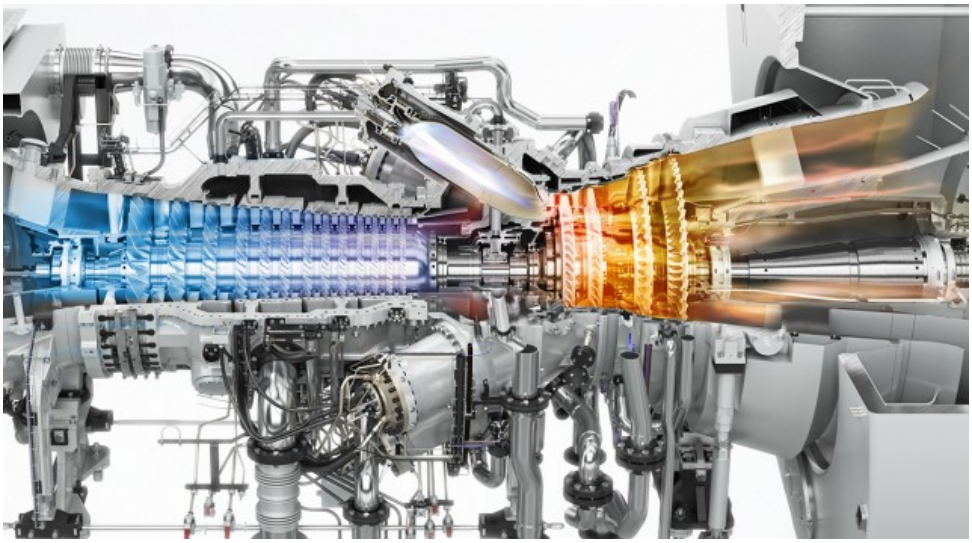

Figure 1.1: SGT-750 gas turbine model, with compressor section colored in blue and turbine section in orange [10]

1.2.1 Burner

The combustion chambers constitutes a fourth-generation Dry Low Emissions (DLE) system [10]. A DLE burner is specifically designed to provide good mixing between fuel and air, and to generate low levels of NO_X and CO in the exhaust gas [11, 12]. A cross section of the burner design is visualized in Figure 1.2, where the DLE burner, the combustion chamber and the transition duct is marked. The SGT-750 burner is equipped with four fuel/air lines; two main inlets, a pilot and a Rich-Pilot-Lean (RPL) stage. The majority of the fuel is injected through the two main channels, where it is distributed into the flowing air through small holes. Thus, the fuel and air rapidly mix in the channels before entering the combustion zone. Guide vanes are placed in both main channels to generate a swirling flow, which is required to obtain a stable flame. Each of the fuel/air liners also has a separate inlet. This increases flexibility, since each inlet can be assigned an individual fuel mix and equivalence ratio. Pre-burned gases enter the combustion chamber through the RPL, which together with the pilot provides further stabilization of the flame. A transition duct is mounted at the converging end of the combustion chamber, which leads the gas flow to the first turbine stage.

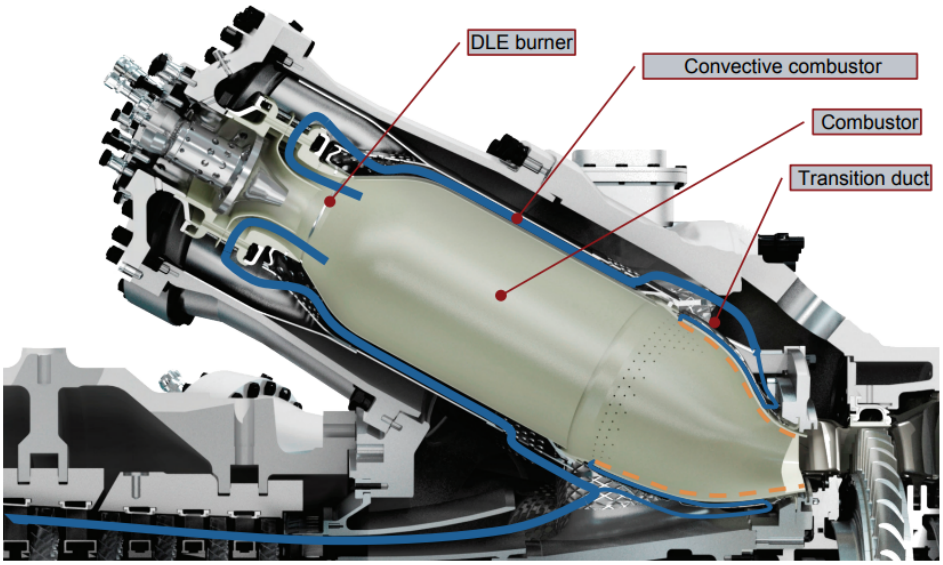

Figure 1.2: Combustion chamber of the gas turbine model SGT-750 [12]. The 4th generation DLE burner, its combustion chamber and the transition duct is marked.

2

Theory

This chapter covers the theoretical background that is needed to grasp the content of this report, including properties of the fuel, emissions and computational models. Resent research work on the topics is presented as well.

2.1 Flame characteristics

To characterize, describe and understand the behavior of a fuel in a combustion process, concepts such as laminar flame velocity (s_L), lower heating value (LHV) and adiabatic flame temperature (T_{ad}) are useful tools. The laminar flame velocity, also known as the laminar flame speed or laminar burning velocity, is the velocity at which the front of a premixed flame propagates, relative to the unburned reactants [13]. The laminar flame speed is defined through equation 2.1

$$s_L = \left(\frac{\alpha \dot{\omega} \ (T_b - T_{ig})}{T_{ig} - T_u} \right)^{1/2} \tag{2.1}$$

where T_u, T_b and T_{ig} are the unburned, burned and self-ignition temperature, respectively. α is the thermal diffusivity of the gas mixture and $\dot{\omega}$ is the reaction rate.

The lower heating value defines the maximum amount of heat that can be released from a specific fuel during combustion, under the assumption that possible fuel moisture and product water is obtained as vapor. This is usually expressed in MJ/kg fuel. Finally, the adiabatic flame temperature is the uniform temperature of a gas mixture that has undergone complete combustion under adiabatic conditions. This temperature is reached when all of the heat released from the combustion process is used to heat the gas. The adiabatic flame temperature and the laminar flame speed are both properties of the fuel, but they also depend on the equivalence ratio and inlet temperature.

2.2 The fuel, its combustion properties and emissions

In this section, the combustion properties of ammonia and hydrogen are explained. Chemical mechanisms available for simulation of combustion are discussed, as well as the formation of emissions in the combustion process and present emission limits.

2.2.1 Characteristics of NH_3 and H_2

Ammonia constitutes a suitable hydrogen carrier due to its much higher boiling temperature compared to pure hydrogen. Ammonia condensates at -33°C at atmospheric pressure, and remains liquefied at room temperature if pressurized to 9.9 atm [14]. This makes transportation and storage of NH_3 much more convenient and cost-effective compared to H_2, which either needs to be heavily pressurized to condensate, or cooled down to -253 °C at atmospheric pressure [15, 3]. However, combustion of pure ammonia is technically challenging due to flame instability issues. This in turn originates from the low chemical reactivity of ammonia, leading to low burning velocities and a larger risk of early blow-off [15]. Ammonia also has a much lower heating value and heat release rate compared to both H_2 and conventional natural gas. The combustion properties of NH_3, H_2 and CH_4 (the main component of natural gas) are summarized in Table 2.1. Here, the maximum burning velocity, $s_{L,max}$, of ammonia is reached at an equivalence ratio of 1.1. A definition of equivalence ratio is given in equation 2.3. Despite its challenges, ammonia has recently gained interest as a potential fuel for electricity generation, also in gas turbine technologies. Although gas turbines in theory are fuel flexible, a switch from methane to ammonia combustion will be a huge challenge. This is primarily due to the large differences between the fuels [6].

	LHV [MJ/kg]	T_{ad}* [K]	Flammability limits, ϕ	$s_{L,max}$ [m/s]
NH_3	18.6	2073	0.63 - 1.40	0.07
H_2	120	2379	0.1 - 7.1	2.91
CH_4	50	2225	0.50 - 1.7	0.37
Fully cracked NH_3	21.3	2255	-	-

Table 2.1: Lower heating value, adiabatic flame temperature, flammability limits and maximum laminar flame speed for ammonia, hydrogen and methane [14]
*Values obtained in this study, for $\phi = 1.0$, T = 300 K, p = 1 bar

In contrast to the low reactivity of ammonia, hydrogen is a highly reactive and fast burning fuel. Adding H_2 or partially cracking the ammonia fuel to its elementary components H_2 and N_2, according to reaction 2.2, is an effective measure to increase the flame speed and flame stability [16, 17]. It must be noted that the process of cracking ammonia to hydrogen is endothermic. Reaction 2.2 demands 2.7 MJ/kg of cracked ammonia (46 kJ/mol) [18], which equals almost 15% of its heating value. However, with a hydrogen content of 17.8% by mass, the gain in LHV of the cracked fuel is enough to overcome the heat demand of the cracking process. As shown in Table 2.1, the LHV of cracked ammonia is exactly 2.7 MJ/kg higher than that of pure ammonia.

$$NH_3(g) \longrightarrow \frac{1}{2}N_2(g) + \frac{3}{2}H_2(g) \tag{2.2}$$

S. Wiseman et al. performed experimental and computational investigations on turbulent combustion of a fuel mixture consisting of 40% NH_3/45% H_2/15% N_2 by volume [6]. This mixture exhibits laminar combustion properties similar to those of

CH_4. Their results showed that, for equivalence ratios $\phi \in (0.3, 0.8)$, the blow-off velocity was about an order of magnitude larger than that of methane. S. Choi et al. performed experimental studies on hydrogen-enriched ammonia flames at elevated temperatures and normal pressure [19]. Their results revealed that the maximum flame temperature and blow-off limits increased for hydrogen-enriched flames, compared to pure ammonia combustion. Thus, H_2 addition has the potential of improving the combustion properties of ammonia flames. M. Ditaranto et al. performed an experimental study on combustion of partially cracked ammonia in a small-scale SGT-750 burner, at different decomposition rates. In their study, fuel mixes of up to 90% ammonia content (by volume) showed strong flame stability at atmospheric pressure [20].

2.2.2 Chemical mechanism

The ability to accurately reproduce experimental results in terms of flame speed, flame structure, emissions and ignition delay time in computational simulations is heavily dependent on the chemical-kinetic mechanism applied to the computational model. Several chemical mechanisms describing both methane- and ammonia combustion have been developed and updated during the past decades [21, 22]. P. Zhang, et al. performed a comparative analysis on various combustion mechanisms for different $CH_4/H_2/CO$/air/diluent-mixes. The predictions of laminar burning velocity by 12 different mechanisms were compared to a collection of experimental data consisting of 5500 data points from 111 different publications [23]. In general, the accuracy of each mechanism was dependent on the operating conditions and fuel composition. However, for operating conditions that are typically present in gas turbine engines, their results pointed towards FFCM-1-2016, SanDiego-2014 and NUIG1.1-2021 as the three mechanisms that succeeded to reproduce the experimental data most accurately. The San Diego mechanism (updated 2016) will be used for simulation of methane combustion in this project.

High accuracy mechanisms often include a complete chemical scheme with hundreds of elemental reactions and species [21, 22]. Implementing such mechanisms would lead to huge computational costs, which inhibit practical usage in computational fluid dynamics models. Instead, short mechanisms have been developed for implementation in computational models. Such mechanisms cover only the reactions and species that influences the combustion characteristics notably. A short nitrogen mechanism on hydrogen-oxygen-nitrogen systems was recently proposed by Y. Jiang et al. [21]. The proposed mechanism is based on the short nitrogen mechanism developed in San Diego during the 1990's, and contains 60 elementary reactions and 19 chemical species. In their study, the laminar burning velocity, extinction strain rate and NO_X emission levels were calculated for different NH_3/H_2 mixes, at equivalence ratios ranging from 0.6 to 1.4. From the mechanism, nitrous oxide profiles were computationally underestimated, while agreeing with experimental data within a factor of 2. Moreover, the ignition delay time was calculated for temperatures ranging from approximately 1600 K to 2500 K, at pressures of 1.4, 11 and 30 atm. The mechanism was shown to reproduce experimental and tabulated data on NH_3/H_2 combustion

properties with high accuracy (± 20%) for high pressures and temperatures. Since high temperatures and pressures are usually found in industrial gas turbines, the mechanism proposed by Y. Jiang et al. is considered appropriate for the current application and will be the primary mechanism used in this project.

Purely kinetic or thermodynamic simulations, such as those performed with Cantera, are less computationally expensive than CFD simulations. This makes such models more compatible with extensive chemical mechanism, such as the one proposed by A. Stagni et. al in 2020 [24]. The mechanism includes 31 species and 203 chemical reactions, and was experimentally validated for oxidation of ammonia under lean conditions ($\phi \leq 0.375$), at temperatures between 500-2000 K and atmospheric pressure. The mechanism was also evaluated by T. Indlekofer et al., who performed chemical reactor network (CRN) and LES simulations on combustion of approximately 5% cracked ammonia in a gas turbine environment, and compared to the San Diego mechanism [4]. Their results showed little difference in the NO_X emissions between the mechanisms. Furthermore, no effect on the N_2O emissions was reported. The Stagni mechanism will be used in this project only for sensitivity analysis of the chemical mechanism on the Cantera model output.

Although the ability of different mechanisms to predict global combustion parameters has been extensively studied, validation of the ability to foresee the production of important individual species such as N_2O is still missing. N_2O is typically formed within the interior of ammonia flames, and decreases in the products after reaching a peak in the primary reaction zone [21]. The need for further experimental validation was specifically pointed out by S.A. Alturaifi et.at., who compared the performance of 15 different chemical mechanisms on ammonia oxidation (including Sandi 2020 but not San Diego), in terms of their ability to numerically reproduce experimental data on N_2O formation during oxidation of ammonia [25]. Their results implied that none of the mechanisms could accurately predict both N_2O mole fraction and peak production time, two crucial characteristics in modelling of N_2O formation. R.C. da Rocha et al. summarized the numerical performance of NO prediction of 10 different chemical mechanisms, through Cantera modeling of ammonia combustion [26]. Their results implied strong variations in the NO emissions between the mechanisms (with peak values ranging from 2800 to 10500 ppm at 1 bar pressure), again pointing out the importance of an accurate chemical mechanism to the performance of numerical simulations on ammonia combustion.

2.2.3 Emissions

If ammonia or ammonia/hydrogen fuel blends are to be implemented as gas turbine fuels, strict control of the NO_X emission rates is required. NO_X formation from hydrocarbon fuels has been thoroughly studied throughout the past decades. However, the formation of NO_X in ammonia combustion differs from that of hydrocarbons since the fuel itself constitutes a source of nitrogen. The formation of NO_X in ammonia/hydrogen combustion has been shown to depend on the equivalence

ratio, fraction of H_2 in the fuel, operating temperature and pressure, and degree of mixing between fuel and oxidizer [1, 4, 20, 27, 28]. A definition of the equivalence ratio is given in equation 2.3 below

$$\phi = \frac{(\dot{m}_{fuel}/\dot{m}_{air})}{(\dot{m}_{fuel}/\dot{m}_{air})_{st}} \tag{2.3}$$

where index *st* refers to the ratio of fuel to air mass flow at stoichiometric conditions. Moreover, humidification of the air flow also reduces NO_X formation, although at the expense of flame stability [1]. In conventional hydrocarbon combustion systems, the only source of nitrogen is air, thus NO_X is mainly formed in regions of high temperature, so called thermal NO_X. In the case of NH_3/H_2 combustion, equivalence ratios above unity have been shown to reduce the level of fuel-NO_X formed in the process [4, 17, 28]. A reduction in NO_X emissions at equivalence ratios close to the lean blow-out limits was also reported by A.A. Kateeb et al., who investigated the stability limits and NO emissions of NH_3/H_2 flames experimentally, at ammonia cracking degrees above 70% and a wide range of equivalence ratios [29].

D. Pugh et al. performed experiments and simulations on NO formation in an ammonia/air diffusion flame and under premixed conditions (ϕ = 0.9-1.2) [1]. They found that the NO production decreased significantly with increasing ϕ, while the amount of NO_2 present in the outlet flow was negligible for all equivalence ratios except $\phi = 0.9$. Z. Li and S. Li performed a numerical study on the effect of mixing on NO_X formation in staged ammonia combustion. In their study, minimum NO_X formation was achieved at $\phi = 1.25$ [27]. Y.Sun et al. performed RANS simulations on combustion of ammonia/hydrogen fuel blends up to 50% H_2 by volume, at equivalence ratios between 0.8-1.4. Their results showed an increase in outlet mole fraction of NO with H_2 fuel content, and a continuous decrease in NO emissions with ϕ.

Rich fuel-oxidizer blends have been proven to reduce NO_X formation, but such blends also leave unacceptable amounts of unburned fuel in the flue gases. Rich-lean staging can be used as a measure of mitigating both NO_X emissions and unburned fuel, simultaneously [4, 1, 27]. In a rich-lean staging process, the combustor is divided into a fuel-rich (low NO_X) and a fuel-lean zone. Secondary air is added downstream of the fuel-rich region to increase the concentration of oxidizer, thus ensuring complete burnout of the fuel. It is important to note that for rich-lean combustors, the NO_X emissions only decrease with primary equivalence ratio up to a certain level. At excessively high equivalence ratios, the level of unburned NH_3 that enters the secondary zone is large enough to generate high levels of NO_X in the secondary zone, thus conquering the emission mitigation obtained by the staging process [27, 30].

For rich-lean staged combustion of NH_3/H_2, larger reductions in NO_X and unburned fuel were found for premixed flames compared to diffusion flames [1]. M. Ditaranto et al. found that for low and medium-high ammonia decomposition rates, minimum NO_X emissions were reached at a local equivalence ratio close to 1.3 [20]. Moreover,

they found that the NO_X emissions increased with the ammonia decomposition rate, apart from the case of full decomposition. The minimum NO_X emission rates were measured to ∼500 ppm for low decomposition rates (< 30% overall, by volume), and close to 1000 ppm for medium-high decomposition rates. Finally, the maximum NO_X level was found at an ammonia decomposition rate of approximately 0.6 at atmospheric pressure, and 0.7 for a pressure of 15 bar ($\phi = 0.9$), indicating that the peak-NO_X decomposition rate increases with pressure. However, their results also showed a dependency of the peak-NO_X decomposition rate on the equivalence ratio. Rich-lean staged ammonia combustion experiments were also performed by Okafor et al., where primary zone equivalence ratios between 0.8-1.4 were investigated. In their study, the minimum NO_X emissions were obtained at $\phi_{PZ} = 1.1$ [30].

Combustion efficiency is another important aspect of a combustion process. In essence, high combustion efficiency is achieved if the gas is fully oxidized at the combustor outlet. The definition of total combustion efficiency, $\eta_{comb,tot}$, used in this report is given in equation 2.4. Under rich conditions, the amount of unburned fuel at the combustor outlet increases with ϕ [28], and hence a second trade-off between low fuel-NO_X and high combustion efficiency is found in ammonia combustion systems.

$$\eta_{comb,tot} = \frac{\dot{m}_{NH_3,in} + \dot{m}_{H_2,in} - (\dot{m}_{NH_3,out} + \dot{m}_{H_2,out})}{\dot{m}_{NH_3,in} + \dot{m}_{H_2,in}} \tag{2.4}$$

2.2.3.1 Emission limits

Sweden is a member of the European Union, where relevant emission limits are provided by the European Union MCP (medium combustion plants) directive. According to the European Union MCP directive (2015), new and already existing gas turbines (1-50 MW_{th}) are obligated to maintain their NO_X emissions below 50 and 150 mg/Nm^3, respectively [31]. Assuming a water content of 16 vol% in the flue gases, the acceptable emission levels can be estimated on a dry basis. The corresponding emissions measured as pure NO or NO_2 are given in Table 2.2. Selective catalytic reduction (SCR) equipment, used for NO_X removal, is typically able to reduce the NO_X emissions by up to 90% [32]. Therefore, the emission limits of a gas flow entering an SCR, which is assumed to reduce the NO_X content by 90%, is also provided in the table.

	NO_X $[mg/Nm^3]$	NO [ppmvd]	NO_2 [ppmvd]
New GT	50	44.5	29.0
New GT with SCR	500	445	290
Existing GT	150	133.4	87
Existing GT with SCR	1500	1334	870

Table 2.2: Maximum allowed NO_X emissions for new and already existing gas turbines, 1-50 MW_{th} [31]

The global warming potential of nitrous oxide is estimated to be between 265 and 298, with a lifetime of 131 ± 10 years [33]. Therefore, the fraction of N_2O that

exits a gas turbine process must be strictly controlled. According to the European Environment Agency, the average CO_2 emissions from electricity generation in the European Union 2020 was approximately 230g CO_2-eq/kWh [34]. For a gas turbine operating with pure methane, with an electrical efficiency equal to that of the SGT-750 gas turbine model (40.3%), the carbon emissions would be approximately 490 g CO_2/kWh. If ammonia shall be considered a competitive fuel despite its challenges, the GWP of the emissions has to be far below that of methane combustion.

2.3 Computational models

This section describes the computational models that are relevant for this project. CFD models and combustion models are explained, as well as their governing equations and how they are implemented in the software STAR-CCM+.

2.3.1 Reynolds-Averaged Navier-Stokes

In the Reynolds-Averaged Navier-Stokes (RANS) framework, transport equations for time-averaged flow quantities are solved. By solving for the mean properties, the RANS framework in general constitutes a computationally affordable method for most engineering applications [35, 36]. However, by time-averaging the instantaneous Navier-Stokes equations, extra terms appear that are mathematically unclosed. The extra terms are turbulent stresses, also known as Reynolds stresses, which must be modeled explicitly to close the governing equations. Hence, turbulent fluctuations are not tracked explicitly in the RANS framework. Instead, it is assumed that any local quantity, ψ, can be decomposed into a sum of its mean and a fluctuating component;

$$\psi = \bar{\psi} + \psi' \tag{2.5}$$

where the bar indicate the time-average of quantity ψ, and the fluctuating component is denoted by a prime [35]. This assumption is applied to the standard Navier-Stokes equations before time averaging. The conservative equations for mass, momentum and energy, as they are implemented in the software STAR-CCM+, are given in equations 2.6, 2.7 and 2.8, respectively.

$$\frac{\partial \rho}{\partial t} + \boldsymbol{\nabla} \cdot \left(\rho \bar{\mathbf{U}}\right) = 0 \tag{2.6}$$

$$\frac{(\partial \rho \bar{\mathbf{U}})}{\partial t} + \boldsymbol{\nabla} \cdot \left(\rho \bar{\mathbf{U}} \bar{\mathbf{U}}\right) = -\boldsymbol{\nabla} \cdot \bar{p}\mathbf{I} + \boldsymbol{\nabla} \cdot \left(\bar{\mathbf{T}} + \mathbf{T_{RANS}}\right) + \mathbf{f}_b \tag{2.7}$$

$$\frac{(\partial \rho \bar{E})}{\partial t} + \boldsymbol{\nabla} \cdot \left(\rho \bar{E} \bar{\mathbf{U}}\right) = -\boldsymbol{\nabla} \cdot \bar{p}\bar{\mathbf{U}} + \boldsymbol{\nabla} \cdot \left(\bar{\mathbf{T}} + \mathbf{T_{RANS}}\right)\mathbf{U} - \boldsymbol{\nabla} \cdot \bar{\mathbf{q}} + \mathbf{f}_b \tag{2.8}$$

Here ρ is the fluid density, $\bar{\mathbf{U}}$ is the mean velocity, $\bar{p}$ is the average pressure, $\bar{E}$ is the mean energy, $\mathbf{I}$ is the identity tensor, and $\mathbf{f}_b$ is the sum of body forces [37]. The stress tensor is composed of two parts; the mean viscous stresses, $\bar{\mathbf{T}}$, and the

turbulent stresses, $\mathbf{T_{RANS}}$, of which the latter has to be modelled. The turbulent stress tensor is defined in equation 2.9

$$\mathbf{T_{RANS}} = 2\mu_t\mathbf{S} - \frac{2}{3}\left(\mu_t\boldsymbol{\nabla}\cdot\mathbf{U} + \rho k\right)\cdot\mathbf{I} \tag{2.9}$$

where μ_t is the turbulent viscosity, $\mathbf{S}$ is the strain rate tensor and k is the turbulent kinetic energy [37]. Finally, for compressible flows an additional closure law is needed - the ideal gas law, equation 2.10,

$$p = \rho RT \tag{2.10}$$

where R is the universal gas constant and T is the temperature.

2.3.2 Turbulence & turbulence models

Turbulence is characterized by the presence of small scale, spatial or temporal, random fluctuations about a large scale mean property in a flow field. The fundamental theory of turbulence is built upon two main principles, of which the first is separation of scales [38]. Turbulent energy is generated at large flow scales and transferred to smaller scales, where the energy is dissipated as heat. The second fundamental principle of turbulence is based on the two Kolmogorov hypotheses. The first hypothesis states that for turbulence at high Reynolds numbers, small scale motions are statistically isotropic, i.e. independent of direction. The second hypothesis states that the turbulent energy field (and thus small scale fluctuations) can be determined through the viscosity and dissipation rate only. This is used to define the smallest scales in a flow - the Kolmogorov scales, given in equation 2.11

$$\eta = (\frac{\nu^3}{\varepsilon})^{1/4} \qquad \tau_\eta = (\frac{\nu}{\varepsilon})^{1/2} \tag{2.11}$$

where η and τ_η are the Kolmogorov length and time scale, respectively [38]. ν is the kinematic viscosity and ε is the dissipation rate. As mentioned in section 2.3.1, turbulence length scales are not resolved in the RANS framework, and hence the turbulent motion must be modelled. Several computational turbulence models exist and are integrated in STAR-CCM+, among them are the two-equation turbulence models; k-ε and k-ω, and the full closure model, Reynolds Stress Transport Turbulence (RSTT). k-ε models are commonly used in engineering applications since they provide a stable and computationally affordable turbulence prediction. The Lag EB k-ε has been shown to impose stability for the specific model of this project and will therefore be integrated in the computational setup.

2.3.2.1 k-ε models

The k-ε model is a turbulent eddy viscosity model that solves for the turbulent kinetic energy, $k = \frac{1}{2}(u_x'^2 + u_y'^2 + u_z'^2)$, and the turbulent dissipation rate, ε, through two primary equations [39]. These two parameters are used to define the turbulent eddy viscosity, μ_t, according to equation 2.12

$$\mu_t = \rho C_\mu \frac{k^2}{\varepsilon} \tag{2.12}$$

where C_μ is a dimensionless constant [35]. Turbulent eddy viscosity models are based on the Boussinesq approximation, which states that the Reynolds stresses are proportional to the mean strain rate. Another important assumption of the classical k-ε model is that of turbulent viscosity isotropy. This assumption is applicable to the bulk flow in many situations, but not to the boundary layers or in strongly rotating flows [38]. Finally, it is assumed that the production and destruction of ε is proportional to that of k, which is essential to avoid non-physical negative values of k [35].

The general k-ε model assumes the stress and strain tensors to be aligned in a flow field, although this is not always the case for highly strained flows [40]. The Lag EB (Elliptic-Blending) k-ε model takes into account possible misalignment between these tensors [41]. An elliptic blending function is also applied to improve low Re near-wall solutions and to reduce the risk to over-predict the production of k [39]. Simultaneously, high accuracy for high Re bulk flows is maintained. The Lag EB k-ε model also provides improved sensibility to anisotropy of turbulence and rotational flows, which are relevant phenomena in gas turbine applications.

In addition to the two parameters k and ε, the Lag EB model solves a transport equation for the reduced, wall-normal stress component, φ, and the elliptic blending factor, α [39]. The turbulent viscosity is modified according to equation 2.13. This equation includes the turbulent time scale, t_t, which is given in equation 2.14.

$$\mu_t = \rho C_\mu \varphi k \min\left(t_t, \frac{C_T}{\sqrt{3} C_\mu \varphi |\mathbf{S}|}\right) \tag{2.13}$$

$$t_t = \sqrt{\left(\frac{k}{\varepsilon}\right)^3 + C_t^2 \frac{\nu}{\varepsilon}} \tag{2.14}$$

Here C_μ, C_T and C_t are model constants and $\mathbf{S}$ is the strain rate tensor. The transport equations solved for the four variables k, ε, φ and α are given in equation 2.15 to 2.18, respectively [37]. The values of all model constant are summarized in Table A.1 in Appendix A.

$$\frac{\partial(\rho k)}{\partial t} + \boldsymbol{\nabla} \cdot \left(\rho k \bar{\mathbf{U}}\right) = \boldsymbol{\nabla} \cdot \left[\left(\frac{\mu}{2} + \frac{\mu_t}{\sigma_k}\right) \boldsymbol{\nabla} k\right] + P_k - \rho(\varepsilon - \varepsilon_0) + S_k \tag{2.15}$$

$$\frac{\partial(\rho \varepsilon)}{\partial t} + \boldsymbol{\nabla} \cdot \left(\rho \varepsilon \bar{\mathbf{U}}\right) = \boldsymbol{\nabla} \cdot \left[\left(\frac{\mu}{2} + \frac{\mu_t}{\sigma_\varepsilon}\right) \boldsymbol{\nabla} \varepsilon\right] + \frac{\varepsilon}{k} C_{\varepsilon 1} P_\varepsilon - C^*_{\varepsilon 2} \rho \left(\frac{\varepsilon^2}{k} - \frac{\varepsilon_0}{t_0}\right) + S_\varepsilon \tag{2.16}$$

$$\frac{\partial(\rho \varphi)}{\partial t} + \boldsymbol{\nabla} \cdot \left(\rho \varphi \bar{\mathbf{U}}\right) = \boldsymbol{\nabla} \cdot \left[\left(\frac{\mu}{2} + \frac{\mu_t}{\sigma_\varphi}\right) \boldsymbol{\nabla} \varphi\right] + \rho \frac{\varepsilon_0 \varphi_0}{k_0} + P_\varphi + S_\varphi \tag{2.17}$$

$$\boldsymbol{\nabla} \cdot \left(L^2 \boldsymbol{\nabla} \alpha\right) = \alpha - 1 \tag{2.18}$$

Here σ_k, σ_ε and σ_φ are model constants, given in Table A.1. P_i is a production term for variable i, and S_i is a user-specified source term for variable i. L is the large-eddy length scale.

2.3.3 Unsteady RANS simulations

As explained in section 2.3.1, the ordinary RANS equations are time-averaged. This means that no large-scale fluctuations are captured. However, it is possible to average over a very short time, to capture unsteady large scale fluctuations also in this framework. This method is called Unsteady Reynolds-Averaged Navier-Stokes (URANS) [36]. To model transient flows in STAR-CCM+, either a user-specified time step or adaptive time stepping can be applied. The adaptive time-stepping tool automatically adjusts the time step size, to meet a user-specified criterion for the temporal resolution [42]. The Courant-Friedrichs-Lewy (CFL) number can be used to define such a criterion, based on the expression below

$$CFL = \frac{u\Delta t}{\Delta x} \leq 1 \tag{2.19}$$

where Δt is the time step and Δx is the cell size [36]. In other words, the time step should be less than, or equal to, the time needed for the convective flow to travel the distance of one cell. The CFL number should be less than one to ensure numerical accuracy and stability. In STAR-CCM+, this is achieved by specifying the target mean value of the CFL number, as well as its target maximum value [42].

2.3.4 Combustion models

Below two types of computational models for combustion are described, as well as the sub models of relevance.

2.3.4.1 Flamelet models

Flamelet combustion frameworks are based on discretization of a large scale turbulent flame into several, local, one dimensional flamelets. The framework is used in computational models for gaseous combustion and provides reduced computational costs compared to frameworks which fully resolve the chemical reactions in time and space [43]. It is assumed that the chemical time scale is much smaller than that of the velocity field, an assumption that decouples the complex chemistry from the flow dynamics [44]. This assumption is generally true for high Damköhler numbers (Da), which describes the ratio of the flow time scale to the reaction time scale. Another fundamental assumption is that the flame thickness is much smaller than the turbulent length scale. This assumption ensures that the local flame structure is not distorted by vertices in the turbulent flow field. Turbulence and its interaction with the flame is instead modeled separately in each flamelet framework.

The flamelet models introduce mixture fraction, Z, as a parameter that determines the local combustion chemistry. The mixture fraction determines the degree of local premixing of the reactants, given in equation 2.20 for component i

$$Z_i = \frac{m_i}{\sum_{k=1}^{n} m_k} \tag{2.20}$$

where m_i is the local mass fraction of stream $i \in (1, n-1)$, and n is the number of streams (eg. fuel, oxidizer and inert) [43]. By solving the transport equation for Z

and its variance, local chemical properties can be obtained. The averaged transport equation solved in STAR-CCM+ is given in equation 2.21

$$\frac{\partial}{\partial t}(\rho\bar{Z}) + \boldsymbol{\nabla} \cdot \left[\rho V - (\rho D_f + \frac{\mu_t}{Sc_Z})\boldsymbol{\nabla} \cdot \bar{Z}\right] = \dot{\omega} \tag{2.21}$$

where V is the volume, D_f is the turbulent diffusivity and Sc_Z is the turbulent Schmidt number for the mixture fraction [43]. $\dot{\omega}$ is a species source term, which is non-zero only if phase changes are present. For steady-state flows, the transient term is set to zero. Tables covering the chemical reaction outcomes and mixture properties as a function of the local thermodynamic state are generated prior to the simulation. As the simulation is initiated, the species mass fractions are interpolated from the tabulated values at each grid point, as a function of the obtained thermodynamic state.

2.3.4.1.1 Flamelet generated manifold The Flamelet Generated Manifold (FGM) model is a sub-model based on the same principles as the general flamelet model, with some differences in the governing equations [45]. The FGM model is suitable for premixed or partially premixed flames. Here, the combustion process is tracked through the introduction of a progress variable, c, which captures the fraction of burned/unburned fuel. Hence, the usually thin film at the flame edge, in which combustion reactions take place, is determined by $c \in (0,1)$ [44]. Various definitions of c exist, however $c = 0$ in the unburned stream. Moreover, flame ignition can be artificially applied in the FGM model, at a user-specified iteration and position.

2.3.4.2 Reacting species transport

In Reacting Species Transport (RST) models, the chemical reactions are no longer decoupled from the flow physics. Instead, a transport equation for each species is solved, and the obtained mass fractions are further processed in a separate chemistry solver to generate the products [46]. This method is used in complex chemistry applications, where the time scale of the reaction kinetics cannot be assumed to be much smaller than that of turbulent mixing. Since the chemical mechanism is modelled explicitly, this method is also useful for modelling flame ignition and quenching. There are several RST sub-models available in STAR-CCM+, however, the Complex Chemistry Model (CCM) is compatible with large chemical mechanisms. Thus, the CCM model is deemed suitable for modelling the kinetics of this specific project.

2.3.4.2.1 Complex Chemistry Model The Complex Chemistry Model solves a system of ordinary differential equations based on the implemented chemical mechanism. The model integrates the chemical mechanism on the time scale of the cell residence time, and can handle a wide range of kinetic time scales within one chemical mechanism [46]. The transport equation solved for each species in the Complex Chemistry Model is given in equation 2.22.

$$\frac{\partial}{\partial t}\left(\rho Y_i\right) + \frac{\partial}{\partial x_j}\left(\rho u_j Y_i + F_{k,j}\right) = \omega_i \tag{2.22}$$

where Y_i is the mass fraction of species i, $F_{k,j}$ represents the diffusion flux and source term, and ω_i is the production rate of species i. Since the effects of turbulence on the chemical production rate is not resolved explicitly, it has to modeled. Modeling turbulence-combustion chemistry interactions is difficult in general, especially at low computational cost [44]. However, there are three models for turbulence-chemistry interactions available in STAR-CCM+, which are all compatible with RANS calculations. The models are the Laminar Flame Concept (LFC) model, the Eddy Dissipation Concept (EDC) model and the Turbulent Flame Speed Closure (TFSC) model [46]. All three models have been previously used to model combustion in industrial applications, such as a methane jet in cross flow [47, 48], Sandia flame D [49] and hydrogen combustion [50]. The TFSC model is however based on the flamelet concept, and requires a correlation for the laminar- and turbulent flame velocities to be specified prior to the simulation. Since no such correlations are available in the literature for the NH_3/H_2 fuel mixes of interest, the TFSC model was deemed unsuitable for this specific project.

The LFC and EDC models define the production rate of species i by equation 2.23

$$\omega_i = \rho f \left(\frac{Y_i^* - Y_i}{\tau} \right) \tag{2.23}$$

where f is the mean reaction rate multiplier, τ is the residence time and Y_i^* is the species mass fraction obtained after integration over a time step [46], see equation 2.25. The LFC model assumes the variable f to equal unity, and the residence time is chosen as the cell residence time. For EDC, the time scale is set equal to the Kolmogorov time scale, equation 2.11, and the variable f is calculated according to equation 2.24,

$$f = \left(\left[C_{l1} \left(\frac{\nu C_{l2} \tau_\eta}{L_t^2} \right)^{0.25} \right]^{-3} - 1 \right)^{-1} \tag{2.24}$$

where C_{l1} and C_{l2} are the fine structure length constant and time constant, respectively [46]. Their default values are given in Table A.2 in Appendix A. L_t is the turbulent length scale. Equation 2.24 typically generates $f < 1$, thus EDC predicts a lower reaction rate compared to LFC. The species mass fraction integration is performed as shown in equation 2.25 for both models.

$$Y_i^* = Y_i + \int_0^\tau r_k \, dt \tag{2.25}$$

Here r_k is the sum of the rates of all reactions that involve species i, based on the respective Arrhenius expressions [46]. Since both the LFC and EDC model explicitly calculates the species production rate, based on the chemical mechanism, both models will be used and compared within this project.

Integrating a complex chemistry solver into a CFD model can be computationally demanding. In STAR-CCM+, the complex chemistry model offers several chemistry acceleration features to reduce computational time, among them the clustering

method [46]. The clustering feature groups cells of similar thermal and chemical state, based on user-specified parameters and clustering limits, and solves for the average properties of the grouped cells. The default clustering parameters for steady solvers are temperature, equivalence ratio, mass fraction of OH, and chemical time scale. For unsteady solvers, temperature, equivalence ratio, and mass fraction of OH are the default clustering parameters. A second acceleration method is the in-situ adaptive tabulation method (ISAT), which tabulates the chemistry ordinary differential equations, and interpolates the solution from the tables.

2.3.5 Cantera

Cantera is an open-source chemical toolbox that provides calculation assistance for problems involving chemical kinetics, thermodynamics and transport processes [51]. In this project, Cantera will be used to simulate chemical reactors and one dimensional flames.

2.3.5.1 Chemical reactors

Chemical reactors can be modelled through Cantera, at either transient or steady state conditions [51]. For steady solutions, a transient reactor is modelled and, starting from specified initial conditions, advanced in time until the solution is converged. Two of the available reactor types are; the zero dimensional ideal gas reactor (also known as perfectly stirred reactor, PSR) and the constant pressure reactor, where the volume and pressure is constant in the respective models. A plug flow reactor is modelled as a series of perfectly stirred reactors. All available reactor models solve for conservation of total mass and species according to equation 2.26 and 2.27, respectively.

$$\frac{dm}{dt} = \sum_{in} \dot{m}_{in} - \sum_{out} \dot{m}_{out} + \dot{m}_{wall} \tag{2.26}$$

$$\frac{d(mY_k)}{dt} = \sum_{in} \dot{m}_{in} Y_{k,in} - \sum_{out} \dot{m}_{out} Y_k + \dot{m}_{k,gen} \tag{2.27}$$

Here m is the mass of the reactor content and $\dot{m}$ in the mass flow [51]. Y_k is the mass fraction of species k. The term $\dot{m}_{wall}$ covers the mass flow due to potential surface reactions (not present herein) and $\dot{m}_{k,gen}$ represents the total generation of species k through chemical reactions. The energy equation is formulated somewhat differently for the different reactor models, however, the ideal gas reactor energy equation is solved for temperature, as given in equation 2.28

$$mc_v \frac{dT}{dt} = -p\frac{dV}{dt} - \dot{Q} + \sum_{in} \dot{m}_{in} \left(h_{in} - \sum_k u_k Y_{k,in} \right) - \frac{pV}{m} \sum_{out} \dot{m}_{out} - \sum_k \dot{m}_{k,gen} u_k \tag{2.28}$$

where h is the enthalpy, and c_v is the heat capacity of the reactor content, at constant volume. $\dot{Q}$ is the heat transfer through the reactor wall, equal to zero for adiabatic processes.

2.3.5.2 1D Flames

There are four types of one dimensional flame models available in Cantera, with the only difference in the modelling parameters being the boundary conditions [51]. The freely-propagating, premixed, laminar and adiabatic flame model will be used to model the burner flame in this project. The conservative equations for mass, radial momentum, energy, and species, solved for a 1D flame in cantera are given in equation 2.29 through 2.32 below

$$\frac{\partial \rho u}{\partial z} + 2\rho\frac{v}{r} = 0 \tag{2.29}$$

$$\rho u\frac{\partial (v/r)}{\partial z} + \rho\left(\frac{v}{r}\right)^2 = -\Lambda + \frac{\partial}{\partial z}\left(\mu\frac{\partial V}{\partial z}\right) \tag{2.30}$$

$$\rho u c_p\frac{\partial T}{\partial z} = \frac{\partial}{\partial z}\left(\lambda\frac{\partial T}{\partial z}\right) - \sum_k j_k c_{p,k}\frac{\partial T}{\partial z} - \sum_k h_k W_k \dot{\omega}_k \tag{2.31}$$

$$\rho u\frac{\partial Y_k}{\partial z} = -\frac{\partial j_k}{\partial z} + W_k\dot{\omega}_k \tag{2.32}$$

where v is the radial velocity, Λ is the pressure eigenvalue, λ is the thermal conductivity, and W_k is the molecular weight of species k [51]. j_k is the diffusive mass flux of species k, which for the multi-component model formulation is calculated according to equation 2.33 below

$$j_k = \frac{\rho W_k}{\bar{W}^2}\sum_i W_i D_{ki}\frac{\partial X_i}{\partial z} - \frac{D_k^T}{T}\frac{\partial T}{\partial z} \tag{2.33}$$

where $\bar{W}$ is the average molecular weight of the gas mixture. D_{ki} is the multi-component diffusion coefficient and D_k^T is the Soret diffusion coefficient [51].

3
Methods

The combustion process was modeled with three different approaches; CFD, CRN and 1D flames. The first part of this chapter describes the geometry, the mesh and the static boundary conditions of the CFD model (section 3.1 and 3.2). Section 3.3 discusses the method development process and different computational setups of the CFD model. Section 3.4 gives the methodology of the CRN and 1D flame simulations performed with Cantera. Finally, section 3.5 shortly describes the approach for post-processing of the results.

3.1 Geometry and mesh

The 30-degree sector model used in this project is shown in Figure 3.1. Here the inlet boundaries and the main outlet are marked with numbers 1-6. The majority of the air enters through the liner- and casing inlets (number 3 and 4 in Figure 3.1 respectively), while only a small part of the total air flow enters through the pilot and RPL (both located at number 5 in Figure 3.1). Similarly, the majority of the fuel enters through main channel 1 and 2 (number 1 and 2 in Figure 3.1 respectively). Only a few percent of the total mass flow of fuel enter though the pilot and RPL, see Table 3.1. All of the gas that enters the combustion chamber exits through the main outlet, indicated by number 6 in Figure 3.1.

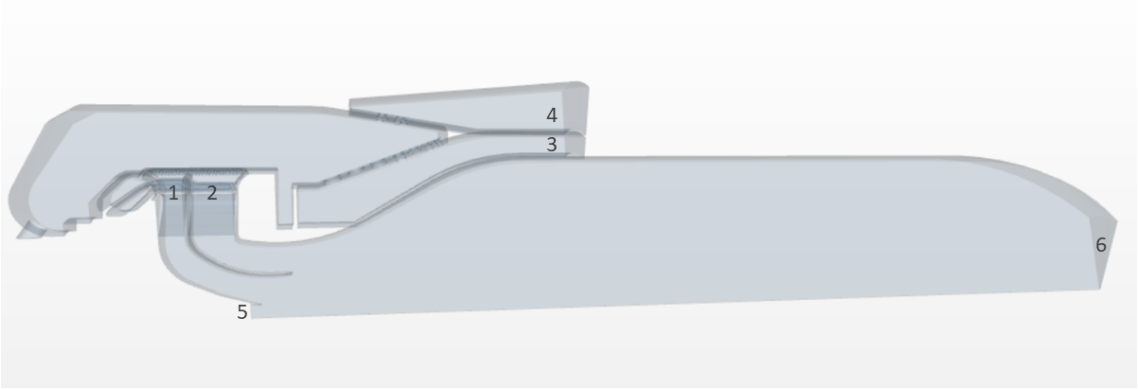

Figure 3.1: 30-degree sector model of the SGT-750 burner used in the simulations. The controlled in-and outlets are numbered as follows; 1) Fuel inlet, main 1. 2) Fuel inlet, main 2. 3) Air inlet, liner. 4) Air inlet, casing. 5) Pilot and RPL inlet. 6) Main outlet.

The mesh consisted of 5.6 million cells in total. Mesh refinements added by M. Safari, S. Reinberth and W. Charoenchang, previously employed at Siemens Energy AB, were covering the main channels and the upper transition region [7, 8, 9]. Further mesh refinements were added to the transition region between the main channels and the combustor, and to the combustor walls close to the DLE burner section. The meshed mid-plane is shown in Figure 3.2, where the darker sections indicate a denser and finer mesh. Since a lot of work was already put into optimizing the burner geometry and its mesh, no further mesh changes were performed in this project.

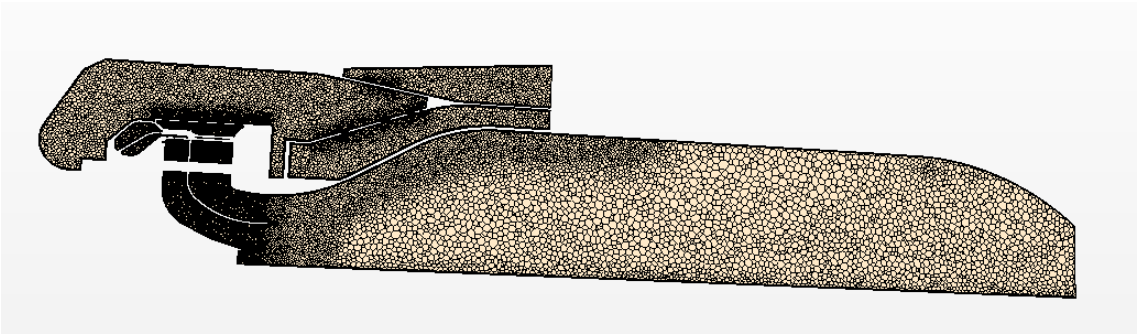

Figure 3.2: Sector model mesh, shown at the 2D mid-plane

3.2 Boundary conditions

The two main inlets for fuel and air were all defined as mass flow inlets. The pilot- and RPL boundary was specified as a velocity inlet, and the velocities were calculated through Cantera (see section 3.4) for each fuel composition. The ratio of mass flow at each boundary inlet to total mass flow was kept constant and is given in Table 3.1. The absolute mass flow of fuel was allowed to vary, while the mass flow of air was kept constant through all simulations. The total mass flow of fuel was adjusted to obtain a constant global flame temperature in the combustor. The normalized inlet temperatures are also provided in Table 3.1, where the base of normalization was set to the air inlet temperature. The temperatures at the RPL and pilot boundaries were not constant in all simulations, hence they are not included in Table 3.1.

	Liner	Casing	Main 1	Main 2	Pilot	RPL
Air mass fraction	0.72	0.25	0	0	0.027	0.0037
Fuel mass fraction	0	0	0.27	0.70	0.03	0.0011
Normalized temperature	1	1	0.38	0.38	-	-

Table 3.1: Normalized total temperature and mass flows at each each boundary inlet

3.3 Development of computational method

The CFD simulations were performed in STAR-CCM+, version 16.06.012-R8. Several computational models and settings for implementation of chemical reactions were tested and evaluated. In this section, the iterative work flow and the various computational models are declared, and their performance is summarized.

3.3.1 Validation of combustion model

The methodology development process was initiated by an overall validation of the geometry and its flow fields under combustion. Comparison of the sector model under methane combustion, using the FGM model and the San Diego mechanism from 2016, against a full scale model of the same burner was performed. This validated the velocity fields, the behaviour of the flame and its position in the sector model. Later, the complex chemistry model was implemented with the same chemical mechanism. Even though the computational cost of the complex chemistry model is much greater compared to the FGM model, the complex chemistry model was chosen primarily to enable the implementation of different fuel compositions at the different inlets, a feature that is not available with the flamelet models.

For complex chemistry modeling, both the EDC and LFC models were tested and evaluated in terms of their ability to reproduce the combustion characteristics obtained for the full-scale model. As mentioned in section 2.3.4.2, the EDC model typically under-estimates the reaction rate compared to LFC. As the EDC model was implemented, no flame was obtained for methane, and neither for the ammonia-hydrogen fuel mix. Hence, it was clear that the underestimation of the reaction rate was large enough to make the EDC model unsuitable for this particular application. However, by implementing the LFC model, a stabilized flame was obtained, and this model was used onwards. This result is in agreement with that of B. Stiehl et al. who simulated turbulent combustion of a jet in cross flow with the RANS framework and the same computational combustion models [47].

3.3.2 Complex chemistry acceleration

To reduce the computation time of the complex chemistry solver, thus enabling a larger number of simulations to be performed withing the time frame of this thesis project, two complex chemistry acceleration features were tested; the clustering method and the ISAT method. For the clustering method, mass fraction of both OH and NO were tested separately as clustering parameters for the steady solver (in addition to the default parameters; chemistry time step, temperature and equivalence ratio), and their effect on the species outlet concentrations was evaluated. Both clustering parameters were shown to reduce the concentration of N_2O by several orders of magnitude compared to the simulations with no clustering. This indicated that the clustering feature is not feasible with the applied chemical mechanism.

The In-Situ adaptive tabulation (ISAT) method was applied as a second option for chemistry acceleration. In contrast to the clustering feature, the ISAT feature over-predicted the concentration of N_2O at the outlet, compared to the simulations without chemistry acceleration. An example of the N_2O variation with chemistry acceleration method is given in Appendix B.3. Since the results to a great extent was dependent on the choice of chemistry acceleration method, the final simulations were performed without such acceleration.

3.3.3 Steady-state monitoring

The RANS framework was used together with the Lag EB k-ε turbulence model. Unfortunately, the steady solver showed great difficulties in convergence. The monitored properties (temperature and species mass fractions) at the outlet were oscillating, with increasing instability for lower ammonia cracking degrees. An example of the oscillating behaviour of a species mass fraction is provided in Appendix B.1. To overcome this problem, two methods were tested and compared; 1) The oscillating data obtained from the steady solver was averaged over 2000 iterations, 2) The unsteady solver (URANS) was selected and a time-average of each parameter was calculated.

The results of the time-averaging method was was shown to be heavily dependent on the time step size. An example of the time-step dependency of N_2O mass fraction is given in Appendix B.2. Therefore, an adaptive time step size was enabled, with a CFL-number below 1. This resulted in a time-step size close to 10^{-7} s. Such a time step demanded a tremendous simulation time, even when initiated from a steady solution. After comparing the results of a steady and an unsteady solution at 30% cracked ammonia, no large differences in the monitored properties at the combustor outlet could be detected. Hence, approach number 1) in the paragraph above was selected for the simulations. The visual attributes of the flame such as shape, position and temperature distribution were, however, not affected by the change of models.

The parameters used to evaluate stability and convergence were; temperature and mass fraction of NO, NO_2 and N_2O, respectively. The named properties were tracked at the outlet boundary, until steady mean values of all parameters were achieved. It was also ensured that the temperature at the outlet was within a range of 10 K from the desired turbine inlet temperature. This ensured that potential differences in emission levels between the simulations were caused primarily by the difference in fuel composition, and not by a difference in combustion temperature.

3.4 Cantera

The python-integrated chemical kinetics tool Cantera was used to generate the boundary conditions of each CFD simulation, and to estimate the adiabatic flame temperature and laminar flame velocity of different fuel mixes. Due to their simplicity and low computational costs, chemical reactor networks and one-dimensional

flames were also used as complementary methods for simulating the combustion process and to find useful trends describing the emissions. The procedures are described in this section. In all simulations, the pressure and combustor outlet temperature were kept constant. The short San Diego mechanism was applied to all Cantera models. To evaluate the effect of the chemical mechanism on the emissions, the Stagni mechanism was also applied to the Cantera models. The results are given in Appendix C.3.

3.4.1 Boundary conditions

All variable boundary conditions of the CFD simulations were generated through Cantera. For the lean combustion cases, the only input variable was mass fraction of cracked ammonia, specified at each of the four inlets. While for rich combustion, equivalence ratio was added as a second input variable. To mimic the introduction of pre-burned gases into the combustor through the RPL, the species mass fractions at the RPL boundary were generated using the *equilibrate* function in Cantera. This function puts the gas mixture to chemical equilibrium at constant enthalpy and pressure [51].

3.4.2 Chemical reactor network model

The combustion process was simulated through a chemical reactor network (CRN) in cantera. The CRN outline is shown in figure 3.3a. The combustion chamber was divided into two sections, a zero-dimensional perfectly stirred reactor (PSR) and a one-dimensional plug flow reactor (PFR). The respective volumes of the two reactors were adjusted to capture the physical flow field properly. The PSR zone was positioned at the flame root, and sized to cover the recirculation zone that appeared in the first part of the combustion chamber. The axial velocity field is shown in figure 3.3b, where the recirculation zone is indicated by the negative axial velocity colored in blue. A recirculating flow field provides enhanced convectional mixing of the gas, which motivates the choice of a PSR at this location. The PFR was positioned downstream of the recirculation zone, where the axial velocity is uniformly directed towards the outlet.

In the PSR zone, the fuel and primary air was assumed to be homogeneously mixed throughout the entire volume, while in the PFR region the gas flow was assumed to be perfectly mixed only in the radial direction. The PFR region was modelled as a series of thin PSR reactors, distributed along the axial coordinate. The secondary air and the PSR outlet flow was mixed prior to entering the PFR region, as shown by the mixing zone in Figure 3.3a. For the simulations without air-staging, the PSR products were assumed to enter the PFR zone directly from the PSR zone, hence not passing the mixing zone. The emission levels of N_2O, NO, and NO_2 were evaluated at the outlet of each reactor zone.

To simulate rich-lean staged combustion also through CFD, a model combining CFD and CRN was set up according to figure 3.4. The exhaust gases from the CFD

simulations were injected into a mixing zone with secondary air before entering a PFR, see Figure 3.4.

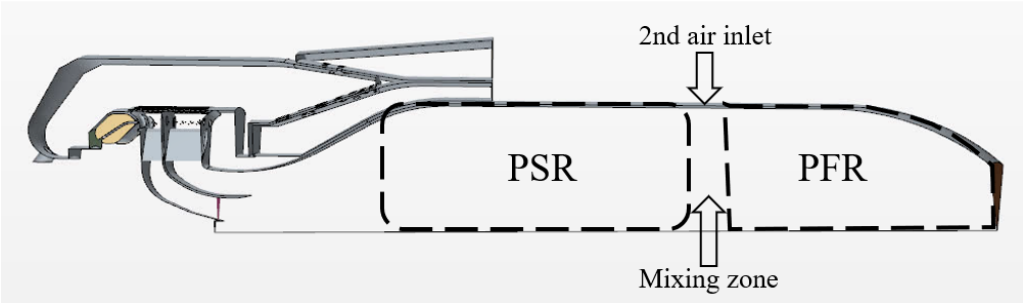

(a) Outline of the chemical reactor network model

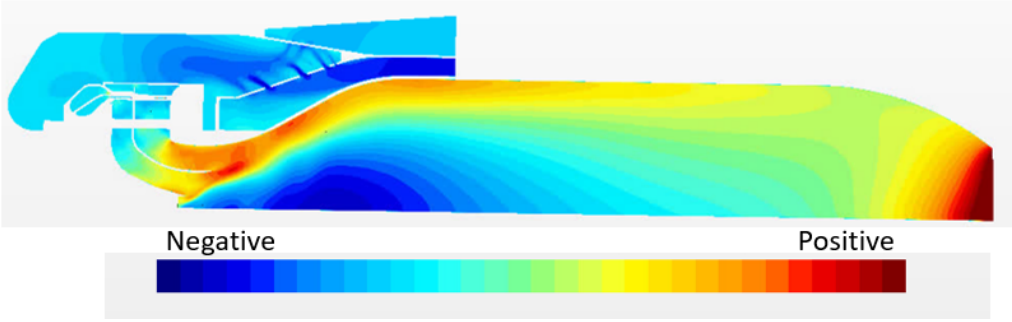

(b) Axial velocity field at the combustor mid-plane

Figure 3.3: Chemical reactor model and axial velocity field at the combustor mid-plane

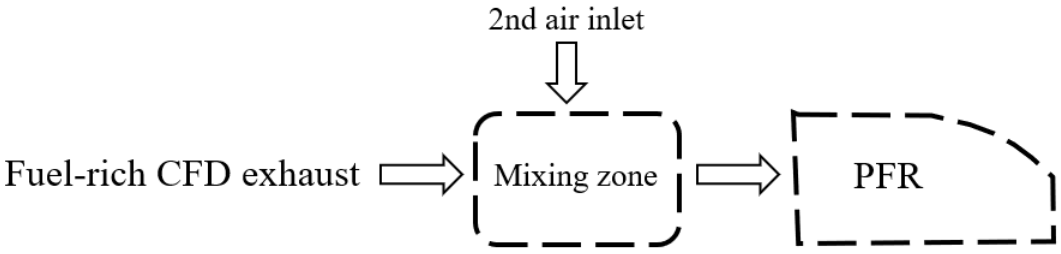

Figure 3.4: Layout of combined CFD and CRN model used for fuel-rich combustion

3.4.3 One-dimensional flames

The air-staged combustion process was simulated by a combination of a 1D flame, a mixing zone and a PFR, according to the layout in Figure 3.5. The 1D flame was assumed to be freely propagating, laminar and adiabatic. The width of the 1D flame was set to 3 mm (in agreement with the flame thickness obtained by Q. Fan et al. [52] for ammonia flames, however slightly in excess of that by Y. Jiang et al. [21] for partially cracked ammonia), and the multi-component transport model

was applied. 1D flames were also used to estimate the laminar flame velocities and adiabatic flame temperatures of different fuel compositions and equivalence ratios.

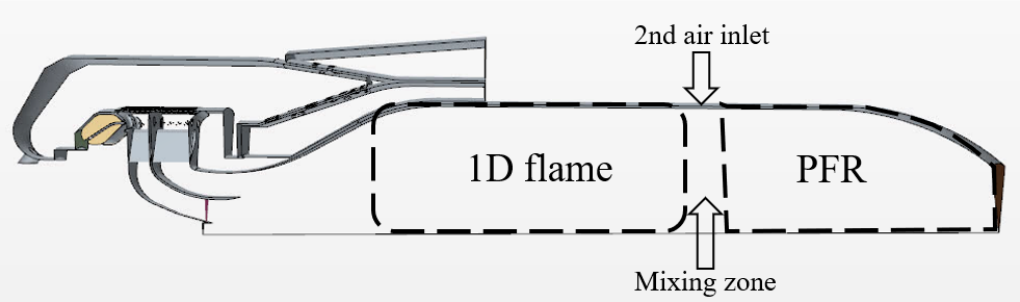

Figure 3.5: Outline of the 1D flame + PFR model

3.5 Post-processing

The temperature, total mass flow and species mass fractions were tracked at the combustor outlet in all of the three methodologies presented. The species mass fractions of NO, NO_2 and N_2O were used to evaluate the emission performance of the combustion, while NH_3 and H_2 were used to evaluate combustion efficiency according to equation 2.4. The emissions were normalized to 15 vol% O_2 on a dry basis, as suggested by C.E. Baukal and P.B. Eleazer [53]. A gas turbine electrical efficiency of 40.3 % was assumed, which is equal to the SGT-750 simple cycle gross efficiency for power generation [10]. The global warming potential of N_2O was assumed to be 298 times that of CO_2, see section 2.2.3.1. The flame stability was evaluated through visualization of the temperature field at the mid-plane of the CFD sector model in STAR-CCM+.

4

Results & Discussion

In this chapter the results of the simulations performed on cracked ammonia combustion are presented and discussed. The chapter is initiated by a presentation of the CRN emissions, followed by the results of the combined 1D flame + PFR model. Later, the CFD results are visualized, and this is followed by a discussion on the differences between the CFD and Cantera models. The estimated flame properties, T_{ad} and s_L, are presented in Appendix D. For air-staged combustion, the cases of fuel-rich conditions in the primary zone, i.e. $\phi_{PZ} > 1$, are referred to as rich combustion, while cases with $\phi_{PZ} < 1$ are referred to as lean combustion. In all simulations, the short San Diego mechanism was applied. The results of the Stagni mechanism are provided in Appendix C.3.

4.1 Chemical reactor network models

This section gives the results of the simulated chemical reactor network. The emissions of the single stage combustion cases are presented, followed by those of air-staged combustion. If not stated otherwise, the pilot and RPL inlets were constantly fed with a fuel mix of 42.8% cracked ammonia by mass. The cracking degree of the main channels ranged from zero to one. Note that all cracking degrees are reported on a mass basis.

4.1.1 Single stage combustion

The total mass flow of fuel was adjusted to maintain the specified global flame temperature. The applied global equivalence ratios are given in Table 4.1 as a function of ammonia cracking degree. The combustion efficiency of all simulations was greater than 99.995% and is thus not reported explicitly.

CD	0.0	0.01	0.1	0.2	0.3	0.4	0.5	0.6	0.7	0.8	0.9	0.99	1.0
ϕ_{global}	0.46	0.45	0.45	0.44	0.43	0.42	0.42	0.41	0.40	0.40	0.39	0.39	0.39

Table 4.1: Global equivalence ratio applied for each fuel composition

Figure 4.1 shows the emission levels of NO_X (NO + NO_2) and N_2O, normalized to 15% O_2 content by volume. The results are given as a function of ammonia cracking degree in the main channels. The global warming potential of the N_2O is given as CO_2 equivalents per kWh of electricity produced. The NO_X emission level increases with CD until it reaches a peak value of 875 ppmvd at CD = 0.8. This NO_X trend

is similar to that obtained by M. Ditaranto et al., whose peak value was obtained at CD = 0.8 by volume (0.67 by mass), at a similar equivalence ratio and 15 bar pressure [20]. As stated in section 2.2.3, the peak-NO_X CD is likely to increase with pressure. Since the combustor pressure in this simulation was fixed at 23 bar, a somewhat higher peak-NO_X CD than that of 15 bar would be expected.

The NO_X emissions were found to be comprised of more than 95 % NO, and hence less than 5% NO_2, on a mass basis. When comparing the calculated NO_X emissions in Figure 4.1 to the NO emissions limits, presented in Table 2.2, it is clear that the emission limits for existing gas turbines could be reached with single stage ammonia combustion, at any cracking degree, if applying additional SCR to the exhaust gas. It should be noted that the NO_X generated at CD = 1.0 is most likely due to the ammonia present in the pilot and RPL, and is not generated from the combustion of hydrogen.

The GWP displayed in Figure 4.1 is lower than that of methane combustion, for all CDs. However, only CD > 0.4 generates a GWP below the EU average of 230 g CO_2-eq/kWh. The maximum N_2O emissions of roughly 100 ppmvd were generated for combustion of pure ammonia, with a corresponding GWP of 434 g CO_2-eq/kWh.

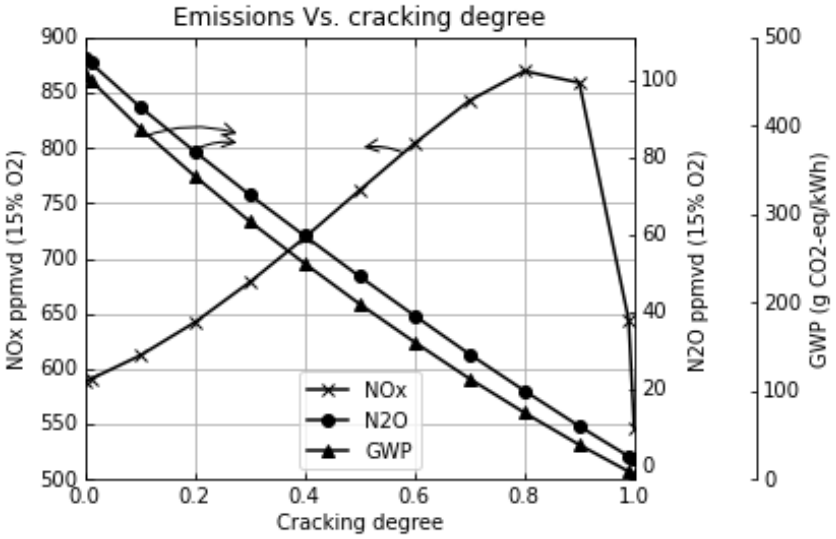

Figure 4.1: NO_X and N_2O emissions from the CRN model, and corresponding CO_2-eq for single stage combustion, as a function of ammonia cracking degree in the main channels

4.1.2 Air-staged combustion

The primary zone equivalence ratio (ϕ_{PZ}) of the air-staged combustion simulations ranged from 0.5 to 1.5. The global equivalence ratio was ensured to match the local equivalence ratio applied to each of the inlets (main 1, main 2, pilot and RPL). The combustion efficiency of all simulations was greater than 99.995% and is not reported explicitly in this section.

Figure 4.2 shows the NO_X emissions from the secondary zone of the chemical reactor network, normalized to 15% O_2 by volume. The graph to the left represents the rich combustion cases ($\phi_{PZ} \in [1.1, 1.5]$), while the graph to the right gives the results of lean and stoichiometric combustion ($\phi_{PZ} \in [0.5, 1.0]$). The trends and emission levels on the lean side agree well with those obtained by M. Ditaranto et al. [20], who found peak-NO_X emissions between 1100-1700 ppmvd at $\phi = 0.9$ (emission levels presented herein are slightly higher due to the constant cracking degree of 42.8% in the pilot and RPL), for a single stage CRN. In figure 4.2 the lowest lean emissions were achieved at $\phi_{PZ} = 0.5$. Note that this is the lowest ϕ_{PZ} presented in the figure, and that both the NO_X emissions and the equivalence ratios of the single stage process (Figure 4.1) are below the minimum of the air-staged combustion. This result indicates a decrease in NO_X emissions as ϕ approaches the lean blow-out limit, as previously reported by A.A Khateeb et al. [29].

The NO_X emissions from lean staged combustion are in general very high, and most cases are not likely to reach the emission limits even with applied SCR. On the other hand, the NO_X trends on the rich side show more promising results compared to the lean side. Here, all combinations of CD and ϕ_{PZ} show the potential of satisfying the NO_X emission limits of 150 ppmvd for existing gas turbines, if combined with SCR. For cracking degrees above 0.4, is could be possible to reach the NO_X emission limits also of new gas turbines. Thus, the results indicate that cracked ammonia under rich-lean staged combustion possesses good potential oas a low emissions gas turbine fuel, for $\phi_{PZ} > 1$. Since the current SGT-750 combustor model is not equipped with a secondary air inlet, substantial geometrical re-design of the current gas turbine engine has to be performed to implement air-staged combustion.

Minimum NO_X emissions of 500 ppmvd were found at $\phi_{PZ} = 1.1$ for pure ammonia. The obtained ϕ_{PZ} is equal to that of E.C. Okafor et al. [30], however the NO_X level is larger by approximately an order of magnitude. The emissions reported in Figure 4.2 are also more than three times those found by K.D.K.A. Somarathne et al. (162 ppm NO), at $\phi_{PZ} = 1.2$, $p = 0.5$ MPa, and CD = 0 [54]. However, the value at ϕ_{PZ} = 1.4 closely matches that obtained by K.D.K.A. Somarathne et al. (891 ppm NO).

The N_2O emission from the secondary zone of the CRN are shown in Figure 4.3, normalized to 15% O_2 by volume on a dry basis. Similar to section 4.1.1, the N_2O-emissions show a negative trend with increasing CD, for all ϕ_{PZ}. The trend with ϕ_{PZ} is positive for rich combustion, while the opposite is true for lean combustion. Hence, to minimize N_2O emissions, the primary zone should be operated close to stoichiometric conditions, independent of fuel composition. The corresponding GWP values are given in Table C.2 in Appendix C.1. It should be stressed that only one combination of CD and ϕ_{PZ} generates a GWP higher than that of methane, namely CD = 0 at $\phi_{PZ} = 1.5$. Moreover, only a few combinations generate a GWP above the average of the European Union (230 g CO_2-eq/kWh). These are found at CD ≤ 0.1 and $\phi_{PZ} = 0.5$, CD ≤ 0.1 and $\phi_{PZ} = 1.4$, as well as CD ≤ 0.3 and ϕ_{PZ} = 1.5. Hence, air-staged combustion of cracked ammonia shows promising potential

as a fuel with low greenhouse gas emissions. To achieve low emission levels of both NO_X and N_2O, the air-staged combustor should thus be operated with $\phi_{PZ} = 1.1$-1.2.

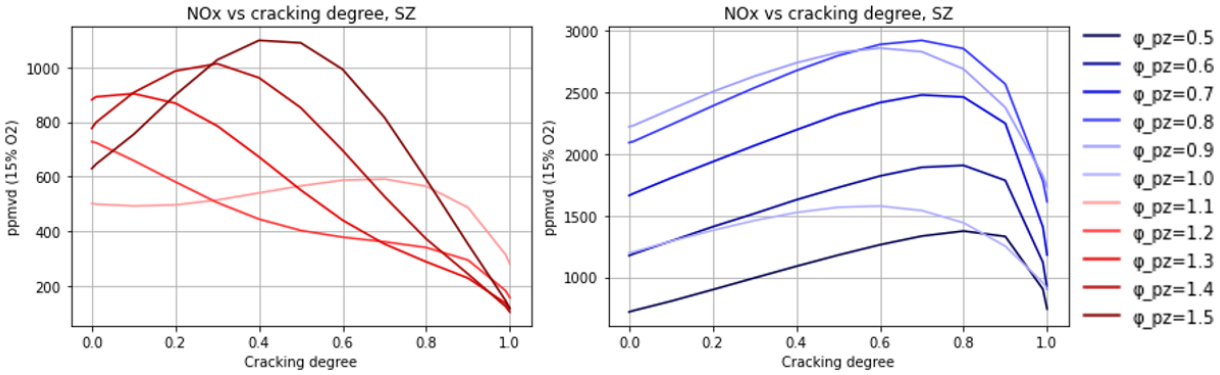

Figure 4.2: NO_X emissions from the air-staged combustion CRN, as a function of CD and ϕ_{PZ}. Rich combustion cases are shown in red (left graph) and lean combustion is shown in blue (right graph)

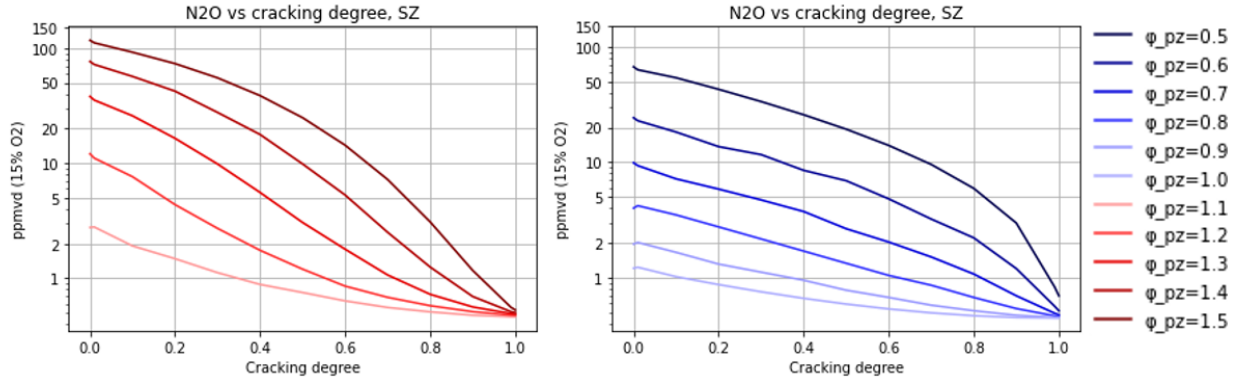

Figure 4.3: N_2O emissions of the air-staged combustion, as a function of CD and ϕ_{PZ}. Rich combustion cases are shown in red (left graph) and lean combustion is shown in blue (right graph)

4.2 One-dimensional flames

The results from the second Cantera model, consisting of a combination of a 1D flame and a PFR, are presented in this section. Firstly, the non-staged combustion results are presented. This is followed by the air-staged simulations. In both cases the ammonia cracking degree ranged from zero to one. The simulations were performed also with the Stagni mechanism, and the results can be found in Appendix C.3. Overall, the two mechanisms produced similar results in terms of NO_X and N_2O emissions. One-dimensional adiabatic flame simulations were also performed to estimate the adiabatic flame temperature and laminar flame velocity of different

fuel compositions. The results are presented and discussed in Appendix D.

Figure 4.4 shows the NO_X and N_2O emissions from the single stage combustion, as a function of cracking degree in the main channels. The NO_X production is similar to that of the CRN model in section 4.1.1, but with a peak-NO_X CD of 0.9 instead of 0.8. The peak-NO_X emission level is also considerably higher compared to the CRN simulation (1270 Vs. 875 ppmvd), thus approaching the emission limit for existing gas turbines. Moreover, the N_2O emissions are below 0.5 ppmvd for all fuel compositions. Hence, from the 1D flame model, the GWP of the flue gases is negligible (not shown here), a result that is not in agreement with the CRN simulations in Figure 4.1. The disagreement between the two models indicate that the N_2O production rate is heavily dependent on the model formulation. In this case, a higher production rate is detected for the CRN model compared to the 1D flame model.

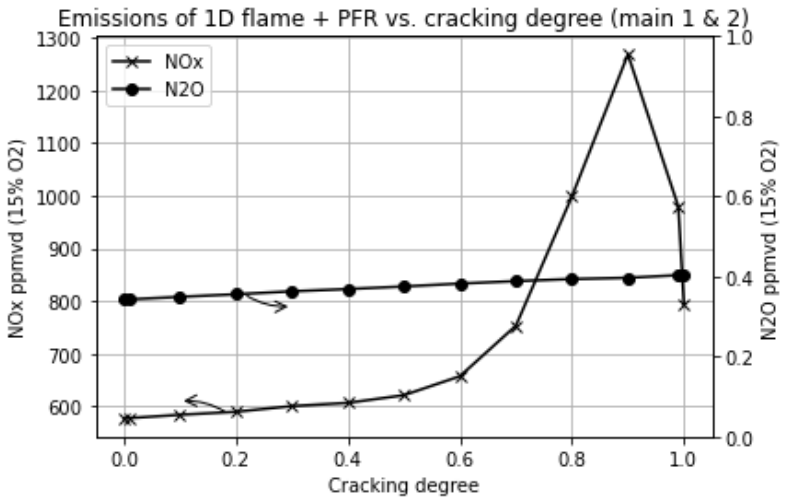

Figure 4.4: NO_X and N_2O emissions of the combined model consisting of a 1D flame and a PFR, as a function of cracking degree in the main inlets

Figure 4.5 shows the NO_X emissions of air-staged combustion, as a function of cracking degree in the main channels and for different equivalence ratios. Cases with a lean primary zone are colored blue, while the rich-lean staged cases are colored red. Similar to the CRN results, the NO_X emissions generated for $\phi_{PZ} < 1$ peaks at $\phi_{PZ} = 0.8$ and CD = 0.8, though at a value of approximately 3800 ppmvd instead of 2900 ppmvd as obtained by the CRN model. The results in Figure 4.5 show overall high levels of NO_X for lean combustion, compared to the desired emission level. With addition of SCR, the cases with potential of reaching the NO_X emission limits for existing gas turbines are those with $\phi_{PZ} = 1.0$, $\phi_{PZ} = 0.5$ at CD < 0.6, and $\phi_{PZ} = 0.6$ at CD ≤ 0.1.

At $\phi_{PZ} > 1$, the NO_X emission levels are below the target of existing gas turbines, at all fuel compositions. Several fuel compositions of high ammonia content show NO_X emissions below 100 ppmvd, a results achieved experimentally by A.A. Khateeb et

al. [29] for ammonia volume fractions of at least 70%.

The results on the rich side, Figure 4.5, agree well with those of the CRN simulations for cracking degrees close to one. However, at lower cracking degrees, the emissions of the 1D flame model are approximately an order of magnitude lower compared to the CRN model. The two simulation techniques also generated significantly different NO_X trends with CD. The lowest NO_X emissions of the 1D flame model were obtained at $\phi_{PZ} = 1.3$, slightly higher than $\phi_{PZ} = 1.1$ as in the CRN model. The trend of the 1D flame model is in closer agreement with the experimental results obtained by M. Ditaranto et al. [20]. Their results showed minimum NO_X emissions at $\phi_{PZ} = 1.3$, though at levels of ~200-800 ppm at cracking degrees up to 30%, as compared to less than 20 ppm reported herein.

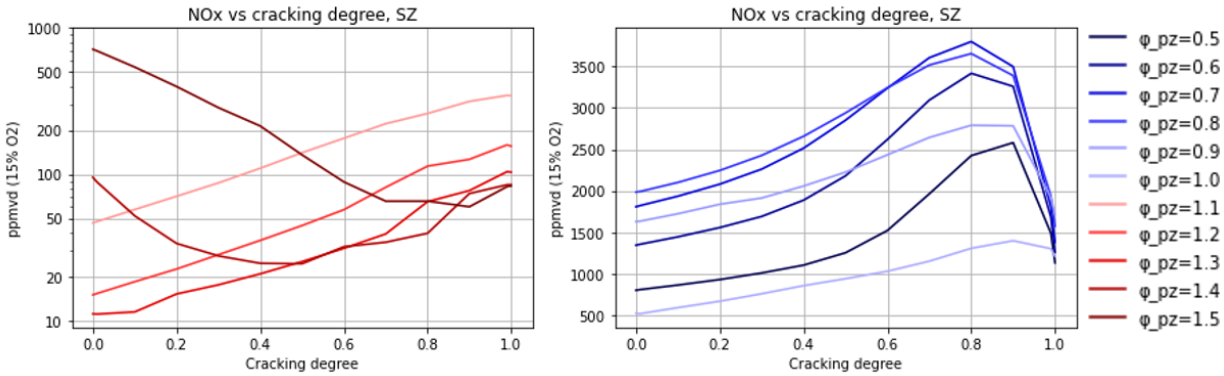

Figure 4.5: NO_X emissions from the combined 1D flame and PFR, as a function of cracking degree and equivalence ratio

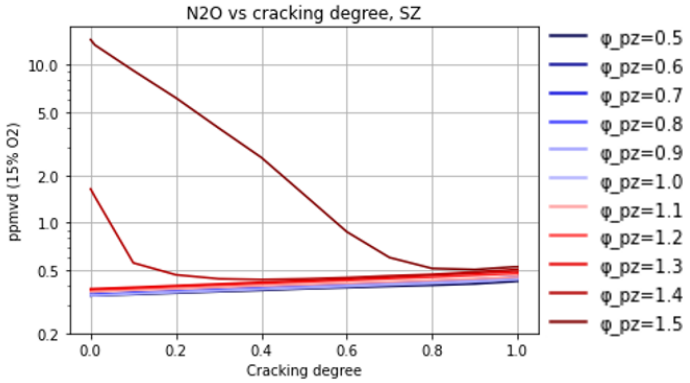

Figure 4.6: N_2O emissions from the combined 1D flame and PFR, as a function of cracking degree and equivalence ratio

The N_2O emissions are shown in Figure 4.6. Almost all cases resulted in N_2O emissions below 1 ppmvd, with a few exceptions at $\phi_{PZ} = 1.4$ and $\phi_{PZ} = 1.5$. Hence, the 1D flame simulations indicate that the N_2O in the exhaust gas are independent of both cracking degree and primary zone equivalence ratio. The corresponding GWP is also negligible. Since this was not the case for the CRN model, it is again

clear that the estimated emissions of N_2O are heavily dependent on the applied chemical model. The results obtained with the Stagni mechanism (Figure C.6a to C.7b in Appendix C.3) also differ from those presented in this section. As already pointed out by S.A. Alturaifi et al. [25] (see section 2.2.3), experimental validation data is required to verify both the computational chemistry models and the chemical mechanism. Moreover, a chemical-kinetic analysis covering the reaction pathways and reaction rates would be useful to, in detail, address the differences between the respective models.

4.3 CFD simulations

This section provides the results of the CFD simulations. Emissions and flame stability of several fuel compositions under lean combustion is discussed, followed by the results of rich combustion. The ammonia cracking degree ranged from zero to 0.99 for lean combustion, and the respective global equivalence ratios are given in Table 4.1. Rich combustion was performed with ammonia cracking degrees between 0.01 and 0.3. CD = 1.0 was not investigated due to assumed practical limitations in the purity of the cracked fuel products.

4.3.1 Lean combustion

Table 4.2 shows the N_2O and NO_X emissions on a dry basis, normalized to 15% O_2 by volume. The table also includes the total mass flow of fuel ($\dot{m}_{norm}$) normalized against the fuel mass flow at pure ammonia combustion, as well as the corresponding GWP of the emitted N_2O in g CO_2-eq/kWh. Combustion efficiencies greater than 99.993% were achiever in all simulations, with the maximum ammonia slip being less than 5 ppmvd.

The required mass flow of fuel decreases with increasing cracking degree (i.e. increasing hydrogen content). This is due to the heating value and adiabatic flame temperature of cracked ammonia being higher than that of pure ammonia, as discussed in section 2.2.1. A higher LHV leads to a greater heat release at full combustion. Hence, for a constant mass flow of air, the temperature can be controlled only through the mass flow of fuel.

The N_2O emissions in Table 4.2 are unacceptably high for ammonia cracking degrees below 0.1. The high N_2O emissions are likely an effect of the flame instabilities seen for the same cracking degrees. This phenomena is visualized in Figure 4.8 and 4.9, and is further discussed in section 4.3.1.1. However, at CD $\geq$ 0.1 the N_2O emissions generate a GWP that is much lower than both that of methane and the EU average. This result is in agreement with the 1D flame + PFR model and indicate that cracked ammonia is competitive as a gas turbine fuel, with respect to greenhouse gas emissions.

The NO_X emissions of the CFD model behaves similar to the 1D flame + PFR model. The peak-NO_X level is found at CD = 0.9, however at a notably higher value of 1795

ppmvd (compared to maximum 1270 ppmvd seen in section 4.2). Apart from the peak at CD = 0.9, the results in Table 4.2 indicate that cracked ammonia has good potential of reaching the NO_X emission limits of existing gas turbines, if combined with additional SCR.

CD (main 1 & 2)	N_2O (ppmvd)	NO_X (ppmvd)	$\dot{m}_{norm}$	CO_2-eq (g/kWh)
0.0	534.2	577	1.0	2308.3
0.05	151.6	610	0.99	653.5
0.1	16.5	626	0.98	70.7
0.15	12.7	639	0.97	54.4
0.2	9.7	611	0.96	40.5
0.3	2.0	640	0.95	8.1
0.4	0.9	642	0.93	3.6
0.5	0.5	652	0.92	2.5
0.6	0.4	655	0.90	1.7
0.8	0.4	1339	0.87	1.6
0.9	0.4	1795	0.86	1.6
0.99	0.4	842	0.85	1.6

Table 4.2: Emissions and normalized mass flow from the CFD simulations, as a function of ammonia cracking degree

4.3.1.1 Flame visualization

The temperature field of a stabilized methane flame is provided in Figure 4.7 and will be used as reference in the evaluation of the visual behavior of the cracked ammonia flames. The temperature fields are used to estimate the flame position, where the parts colored in red can be assumed to enclose the flame. The flame front will be referred to as the yellow transition region, in which the temperature transfers from green to red. The flame in Figure 4.7 is stabilized, and characterized by the position of the flame root (with sufficient distance to the inlets to avoid flashback), its thin flame front, and a uniform temperature distribution in the combustion chamber.

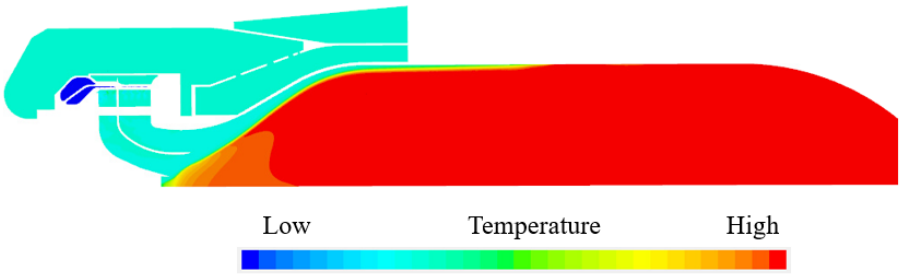

Figure 4.7: Temperature field of methane combustion

The normalized temperature fields of the lean, single stage ammonia combustion simulations are shown in Figure 4.8. Here, the temperature has been normalized with respect to the maximum temperature present among the lean flames. The

cracking degree of the fuel in the main channels is specified to the right of each picture. From Figure 4.8, a lower CD seems to generate a more stretched flame compared to the flame in Figure 4.7. This is indicated by the axial coordinate at which the upper flame edge reaches the wall, and by the distance between the flame edge and the burner wall. A stretched flame may cause enhanced instability and a risk of incomplete chemical reactions, leading to a negative effect on the turbine efficiency and a risk of finding impurities in the gas as it enters the turbine. It should also be noted that the flame fronts in Figure 4.8 are visually thicker than that of the methane flame in Figure 4.7, for low cracking degrees. The wider flame front is most likely caused by computational instabilities, and does not indicate that the actual thickness of the ammonia flames is greater than that of a methane flame. This could however indicate that the flame is characterized by geometrical fluctuations, which causes smearing of the flame front in the time-averaged RANS solution.

At 40-70% cracked ammonia, the flame closely resembles the methane flame. The thickness of the temperature gradient between the unburned and burned gases is thin compared to the cases with lower cracking degree, indicating a less fluctuating behavior of the flame front. This gives an indication of high flame stability for cracking degrees of at least 40% in the two main channels. This result is in line with the experimental results reported by Wiseman et al., who found similar combustion properties of a 40% NH3/45% H2/15% N2 fuel mixture (which corresponds to 42.8% cracked ammonia by mass) as for pure methane combustion, see section 2.2.1. At CD > 0.7, the flame front is positioned upstream of the methane flame, indicating an increased risk of flashback. Local high temperature spots are also apparent close to the chamber wall at higher cracking degrees, likely a consequence of a higher concentration of hydrogen in the fuel.

The normalized N_2O mass fraction fields of eight selected simulations of varying cracking degrees are shown in figure 4.9. The fields have been normalized with respect to the maximum N_2O mass fraction present among the lean flames. Since N_2O is typically formed in the interior of the flame, its mass fraction field is used to estimate the position of the primary reaction zone. Again, the degree of ammonia cracking is indicated by the numbers in the figure. As the flame length increases for decreasing CD, so does the length of the reaction zone, and vice versa. For pure ammonia combustion, the reaction zone is stretched completely to the combustor outlet. The region of high mass fraction of N_2O (i.e. the red/yellow parts of Figure 4.9) reaches entirely to the outlet plane, which causes the large N_2O mass fraction seen in Table 4.2. Hence, the N_2O emissions can be attributed primarily to flame instability. This phenomena was previously noticed by S. Mashuk et al. [5] in their experimental study, where both ammonia slip and N_2O emissions could be strongly related to instability of the flames. Therefore, cracking degrees much greater 10% should be applied to mitigate N_2O emissions. It should be noted that neither flame instabilities nor incomplete combustion (under lean conditions) is captured in any of the two Cantera models, which partly explains the differences seen between the CFD simulations and the Cantera models.

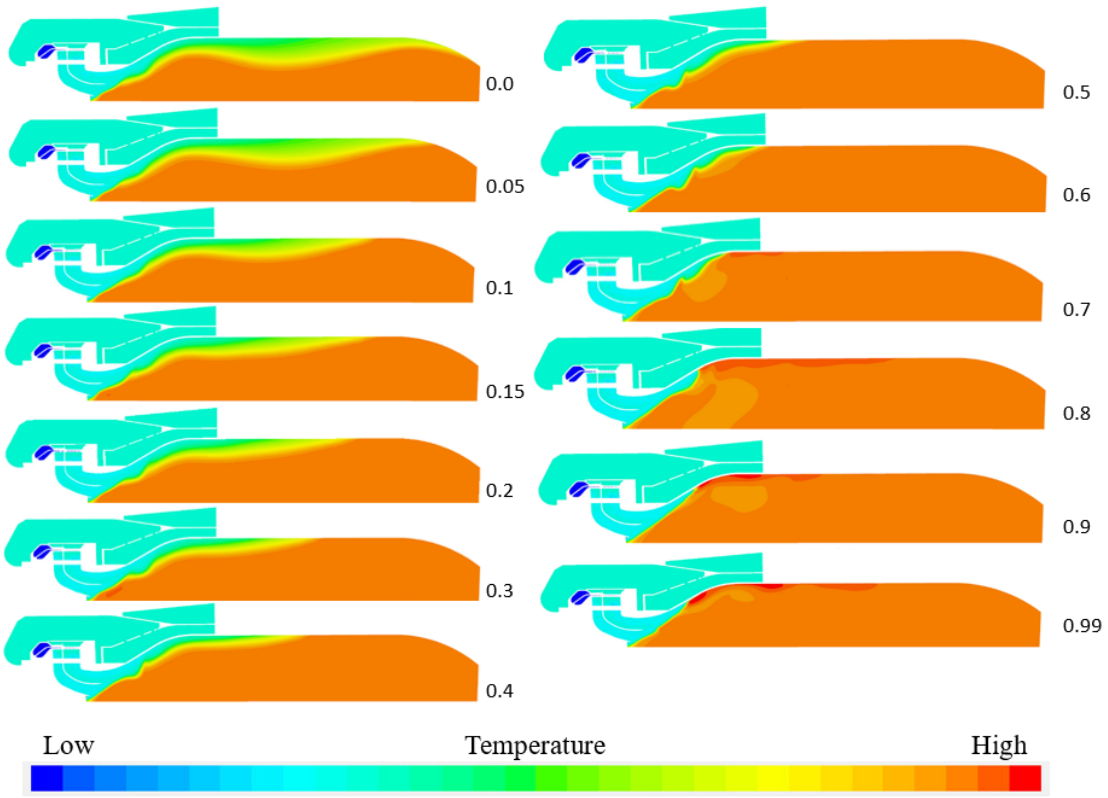

Figure 4.8: Normalized temperature field of several different fuel mixes, with numbers indicating the decree of cracking in each temperature field

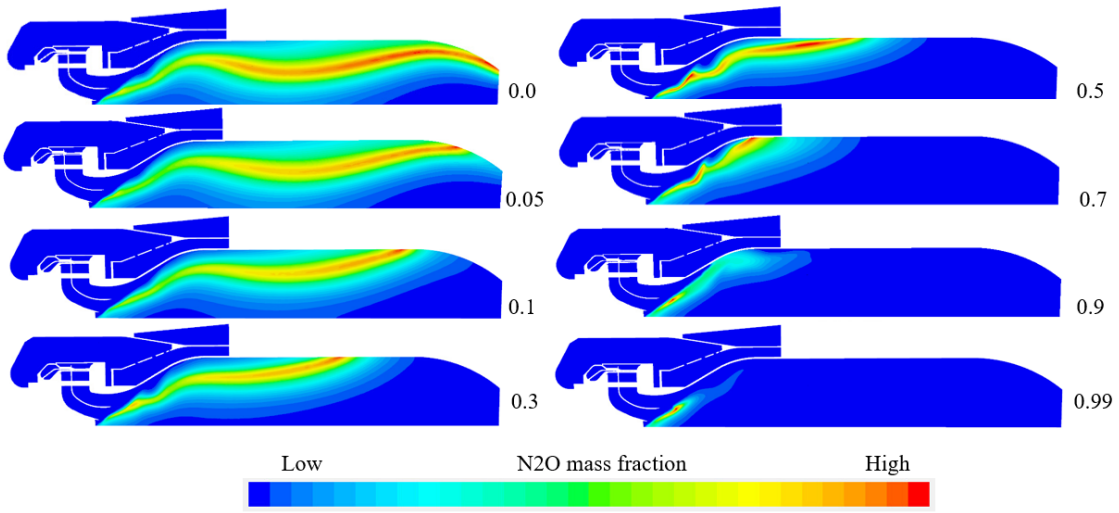

Figure 4.9: Normalized distribution of N_2O mass fraction for different fuel mixes, with numbers indicating the decree of cracking in each picture

It was also investigated whether the flame instability observed for low degrees of cracked ammonia could be improved by combining globally lean with locally rich

conditions. Figure 4.10 shows the normalized temperature field and N_2O mass fraction of 10% cracked ammonia (main 1 and 2), under such combined conditions. The pilot and RPL were operating at locally rich conditions, $\phi_{pilot+RPL} = 1.1$, while the main channels were locally lean, at $\phi_{main1+2} = 0.5$. These conditions generated a globally lean flame, but required a small amount secondary air to obtain the desired combustor outlet temperature.

If compared to the flame of 10% cracked ammonia in figure 4.8, the flame stability is improved by the implementation of rich conditions in the pilot and RPL. Since the global equivalence ratio is somewhat higher than that of figure 4.8, a higher global temperature is also seen in Figure 4.10. With addition of secondary air, NO_X emissions of 918 ppmvd were obtained, an increase compared to 626 ppmvd obtained for the same cracking degree at fully lean combustion (Table 4.2). This is however still below the emission limit of existing gas turbines, if the process is combined with SCR. Only 0.4 ppmvd of N_2O were emitted, which corresponds to a GWP of 1.6 g CO_2-eq/kWh.

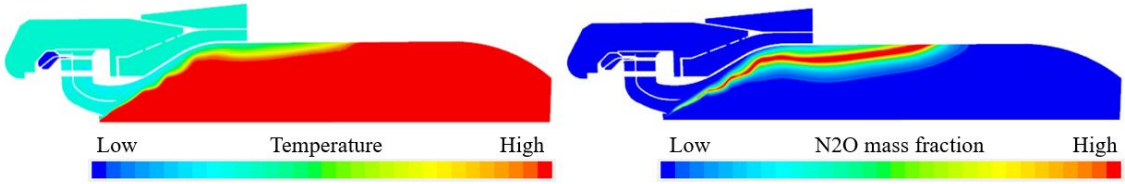

Figure 4.10: Normalized temperature field and N_2O mass fraction of 10% cracked ammonia, at $\phi_{main1+2} = 0.5$ and $\phi_{pilot+RPL} = 1.1$

4.3.2 Rich combustion

The emissions of NO_X and N_2O, and the corresponding GWP in terms of CO_2-equivalents, from the combined CFD + PFR model are given in Table 4.3 for ammonia cracking degrees between 0.01 and 0.3. The local and global primary zone equivalence ratios were both set to 1.1. The NO_X and N_2O emissions detected at the outlet of the combustor in the CFD model, before addition of secondary air, are provided in Appendix E.1.

The NO_X and N_2O emissions in Table 4.3 are in good agreement with those reported from the 1D flame + PFR model. Both models generated NO_X emissions levels below 100 ppmvd for CD $\leq$ 0.3 and N_2O emissions around 0.5 ppmvd.

As reported in the literature (section 2.2.3), the results show that rich-lean staging can be used to mitigate NO_X emissions compared to lean combustion. With this method, combustion of ammonia shows potential of reaching the NO_X emission limits without additional SCR. Moreover, the constantly low N_2O emissions indicate that rich-lean staged combustion of cracked ammonia has very low greenhouse gas emissions. Similar results were observed for ~5% cracked ammonia by T. Indlekofer

et al., in terms of both NO_X (330 mg/MJ) and N_2O (0.2 ppm) emissions [4].

CD (main 1 & 2)	N_2O SZ (ppmvd)	NO_X SZ (ppmvd)	CO_2-eq (g/kWh)
0.01	0.4	51.4	1.6
0.01 (pilot + RPL 0.1)	0.4	54.1	1.6
0.1	0.4	58.3	1.6
0.2	0.4	72.8	1.6
0.3	0.4	80.6	1.6

Table 4.3: Emissions from the combined CFD + PFR model at $\phi_{PZ} = 1.1$

Figure 4.11 shows the temperature field of four rich flames, normalized to the maximum temperature present within the rich flames. The numbering gives the ammonia cracking degree applied in each picture. As expected from the adiabatic flame temperatures in Figure D.2, Appendix D, the global flame temperature increases with CD. All of the flames show high flame stability, indicated by the thin flame fronts. With increasing CD, the flame front stabilizes closer to the main inlets, enhancing the risk of flashback. Note that the risk of flashback is enhanced at lower cracking degrees compared to the lean cases. This is primarily due to a reduced mass flow of air, required to obtain the specified equivalence ratio.

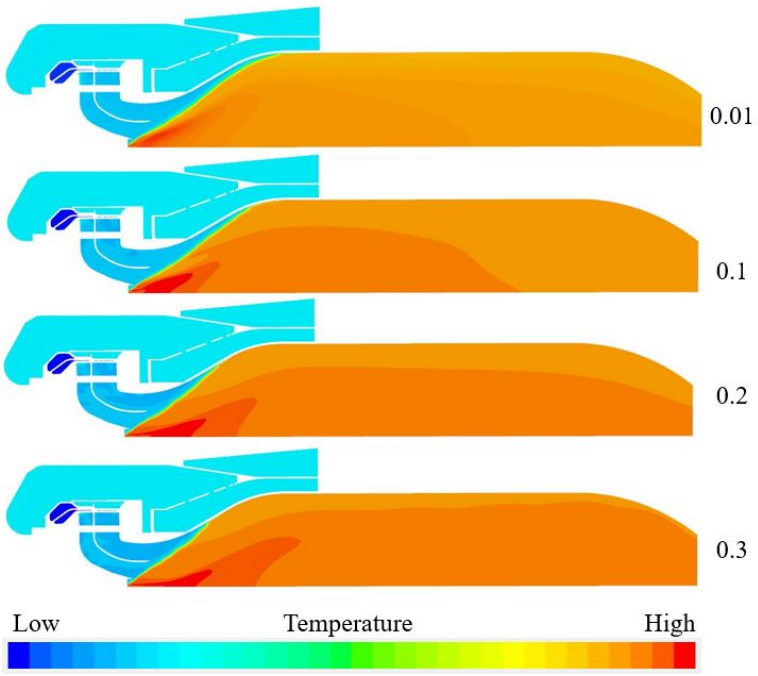

Figure 4.11: Normalized temperature fields of $\phi_{PZ} = 1.1$, with ammonia cracking degree between 0.01 and 0.3, as numbered in the figure

4.4 Model remarks

It should be stressed that the CRN provides a simplified model of the combustion process. In the CRN model, it is assumed that the main combustion reactions take place within the PSR region. However, based on the visual results of Figure 4.9, the reaction zone spans over a much larger volume than anticipated in the CRN model, particularly at low cracking degrees. Moreover, the CRN model assumes the gas to be homogeneously mixed, and thus that the reactions take place at equal rates in the entire PSR volume. From Figure 4.9, this is clearly not the case. Instead, the 1D flame model seems to give a better estimation of the reaction zone geometry displayed by the CFD simulations. However, both models fail to capture the geometrical distribution of the reaction zone for CD < 0.1. They also fail to predict the effects of flame instability on the combustion process. Moreover, the 1D flame is assumed to be freely-propagating, flat and laminar, while flames in a gas turbine combustor are actually highly strained and turbulent.

5
Conclusion

Combustion of cracked ammonia in the gas turbine model SGT-750, provided by Siemens Energy AB, was modelled through CFD and two different python-integrated Cantera models. NO_X and N_2O emissions were evaluated, as well as global warming potential and flame stability. The models covered a 30°sector of the full combustion chamber, and CFD simulations were performed with the RANS framework in combination with complex chemistry. The chemical mechanism proposed by Y. Jiang et al. was applied [21]. The first Cantera model constituted a chemical reactor network model consisting of a perfectly stirred reactor and a plug flow reactor (CRN model). In the second model, a one-dimensional flame was combined with a plug flow reactor to represent the combustion process (1D flame model). All models were applied both to single stage and air-staged combustion. Investigated ammonia cracking degrees ranged from zero to one. Equivalence ratios of approximately 0.4 were applied to single stage combustion, while primary zone equivalence ratios between 0.5 and 1.5 were investigated in air-staged combustion through the two Cantera models. Rich CFD simulations were performed with a primary zone equivalence ratio of 1.1.

Flame stability was evaluated from the temperature fields of the CFD model. At lean conditions, flames with a low degree of cracked ammonia were characterized by instability and prolonged reaction zones. However, stability was achieved for lean flames at cracking degrees of 40% and above. For 80% cracked ammonia and above, an increased risk of flashback was observed. Under fuel-rich conditions, no instability tendencies were observed. However, the risk of flashback was enhanced already at 20% cracked ammonia.

All three models showed promising NO_X emission levels of single stage combustion, with the majority of the emission levels between 500-800 ppmvd. This results shows strong potential of reaching the NO_X emission limits of the European Union, if combined with selective catalytic reduction techniques. The NO_X emissions increased with ammonia cracking degree until a peak was reached, and decreased close to fully cracked ammonia, a trend observed also by M. Ditaranto et al. [20]. A peak-NO_X level of 875 ppmvd was obtained at 80% cracked ammonia in the CRN model. The 1D flame and the CFD model generated peak-NO_X emissions of 1270 and 1795 ppmvd, respectively, both at 90% cracked ammonia.

For lean, air-staged combustion ($\phi_{PZ} \in [0.5, 1.0]$), the NO_X emissions were found to increase with primary zone equivalence ratio, as reported previously by E.C. Okafor et.al [30] and M. Ditaranto et al. [20]. Peak-NO_X cracking degrees were found be-

tween 0.6 and 0.8 with the CRN model. The 1D flame model generated peak-NO_X cracking degrees between 0.8 and 0.9, while slightly overestimating the peak-NO_X value compared to the CRN model. In general, high NO_X emissions were generated for air-staged combustion with a lean primary zone, in the range of approximately 1000-3000 ppmvd.

Combustion of ammonia in a fuel-rich primary zone was shown by all three models to reduce the NO_X emission levels compared to a fuel-lean primary zone, as previously reported in the literature [4, 5, 20, 30]. However, the two Cantera models generated significantly different trends regarding the dependency of NO_X on the cracking degree and the equivalence ratio. From the CRN model, a primary zone equivalence ratio of 1.1-1.2 was shown to generate low NO_X and low N_2O emissions simultaneously. The lowest emissions of the 1D flame model were instead generated at ϕ_{PZ} between 1.3-1.4, which better agrees to the results of M. Ditaranto et al. [20]. The differences in emission levels between the two models were about an order of magnitude for lower cracking degrees, while similar emissions were predicted by both models at fully cracked ammonia.

A great discrepancy between the models was also observed for the trends of N_2O emissions with cracking degree and equivalence ratio. From the CRN model, N_2O decreased constantly with ammonia cracking degree, with the lowest N_2O emissions generated at stoichiometric conditions and fully cracked ammonia. In contrast to the CRN model, the results of the 1D flame model indicated that the N_2O emissions were instead independent of both ammonia cracking degree and equivalence ratio. The model also showed a negligible global warming potential of the combustion process, with N_2O emissions between 0.4-0.5 ppmvd. Such low N_2O emission were generated also from the stable flames of the CFD model, for ammonia cracking degrees above 10%. The results agree to those obtained by T. Indlekofer et al. [4] and S. Mashruk et al. [5]. Finally, N_2O formation was shown to be highly dependent on the computational chemistry model and its settings. The observed discrepancy in the prediction of N_2O formation implies a requirement of experimental data for validation of the computational models and the chemical mechanism, as previously observed by S. Alturaifi et al. [25]. A chemical-kinetic analysis of the models is also required to fully address the differences between the models.

Bibliography

[1] Pugh D, Valera-Medina A, Bowen P, Giles A, Goktepe B, Runyon J, et al. GT2020-14953 EMISSIONS PERFORMANCE OF STAGED PREMIXED AND DIFFUSION COMBUSTOR CONCEPTS FOR AN NH3/AIR FLAME WITH AND WITHOUT REACTANT HUMIDIFICATION; 2020.

[2] Patonia A, Poudineh R. Ammonia as a storage solution for future decarbonized energy systems. Oxford Institute for Energy Studies; 2020.

[3] Valera-Medina A, Xiao H, Owen-Jones M, David WIF, Bowen PJ. Ammonia for power. Elsevier Ltd; 2018.

[4] Indlekofer T, Gruber A, Wiseman S, Nogenmyr KJ, Larfeldt J. GT2022-83131 NUMERICAL INVESTIGATION OF RICH-LEAN STAGING IN SGT-750 SCALED DLE BURNER WITH PARTIALLY-DECOMPOSED AMMONIA; 2022.

[5] Editors G, Shiun Lim J, Alafiza Yunus N, Jaromír Klemeš J, Mashruk S, Kovaleva M, et al. Nitrogen Oxides as a By-product of Ammonia/Hydrogen Combustion Regimes. In: CHEMICAL ENGINEERING TRANSACTIONS. vol. 89; 2021. p. 2021. Available from: `www.cetjournal.it`.

[6] Wiseman S, Rieth M, Gruber A, Dawson JR, Chen JH. A comparison of the blow-out behavior of turbulent premixed ammonia/hydrogen/nitrogen-air and methane–air flames. Proceedings of the Combustion Institute. 2021 1;38(2):2869–2876.

[7] Safari M. Geometrical improvement of SGT-750 burner-Main Channels 1 and 2. Linköping: Linköpings universitet; 2020. Available from: `www.liu.se`.

[8] Reinberth S. Method to optimize burner fuel holes locations. Finspång; 2020.

[9] Charoenchang W. Analysis of Fuel-Air Mixing in Jet in Crossflow. Gothenburg: Chalmers University of Technology; 2021. Available from: `www.chalmers.se`.

[10] Siemens Energy. SGT-750 Industrial gas turbine;. Available from: `https://www.siemens-energy.com/global/en/offerings/power-generation/gas-turbines/sgt-750.html`.

[11] Boyce MP. Combustors. In: Gas Turbine Engineering Handbook. Elsevier; 2012. p. 427–490.

[12] Hellberg A. THE SIEMENS SGT-750 GAS TURBINE: DEVELOPED FOR THE OIL AND GAS INDUSTRY;.

[13] Andersson S, Bengtsson PE, Leckner B, Pallarès D. COMBUSTION ENGINEERING MEN031 7.5 ECTS. Thunman H, editor. Gothenburg: Reproservice, Chalmers University of Technology; 2020.

[14] Kobayashi H, Hayakawa A, Somarathne KDKA, Okafor EC. Science and technology of ammonia combustion. Proceedings of the Combustion Institute. 2019;37(1):109–133.

[15] Wei X, Zhang M, An Z, Wang J, Huang Z, Tan H. Large eddy simulation on flame topologies and the blow-off characteristics of ammonia/air flame in a model gas turbine combustor. Fuel. 2021 8;298.

[16] Osipova KN, Zhang X, Sarathy SM, Korobeinichev OP, Shmakov AG. Ammonia and ammonia/hydrogen blends oxidation in a jet-stirred reactor: Experimental and numerical study. Fuel. 2022 2;310.

[17] Bioche K, Bricteux L, Bertolino A, Parente A, Blondeau J. Large Eddy Simulation of rich ammonia/hydrogen/air combustion in a gas turbine burner. International Journal of Hydrogen Energy. 2021 11;46(79):39548–39562.

[18] Thomas G, Parks G. Potential Roles of Ammonia in a Hydrogen Economy - A Study of Issues Related to the Use Ammonia for On-Board Vehicular Hydrogen Storage. U.S. Department of Energy; 2006.

[19] Choi S, Lee S, Kwon OC. Extinction limits and structure of counterflow non-premixed hydrogen-doped ammonia/air flames at elevated temperatures. Energy. 2015 6;85:503–510.

[20] Ditaranto M, Larfeldt J. EXPERIMENTAL STUDY ON HIGH PRESSURE COMBUSTION OF DECOMPOSED AMMONIA: HOW CAN AMMONIA BE BEST USED IN A GAS TURBINE?; 2021. Available from: http://asmedigitalcollection.asme.org/GT/proceedings-pdf/GT2021/84959/V03BT04A027/6757779/v03bt04a027-gt2021-60057.pdf.

[21] Jiang Y, Gruber A, Seshadri K, Williams F. An updated short chemical-kinetic nitrogen mechanism for carbon-free combustion applications. International Journal of Energy Research. 2020 2;44(2):795–810.

[22] Otomo J, Koshi M, Mitsumori T, Iwasaki H, Yamada K. Chemical kinetic modeling of ammonia oxidation with improved reaction mechanism for ammonia/air and ammonia/hydrogen/air combustion. International Journal of Hydrogen Energy. 2018 2;43(5):3004–3014.

[23] Zhang P, Zsély IG, Papp M, Nagy T, Turányi T. Comparison of methane combustion mechanisms using laminar burning velocity measurements. Combustion and Flame. 2022 4;238.

[24] Stagni A, Cavallotti C, Arunthanayothin S, Song Y, Herbinet O, Battin-Leclerc F, et al. An experimental, theoretical and kinetic-modeling study of the gas-phase oxidation of ammonia. Reaction Chemistry and Engineering. 2020 4;5(4):696–711.

[25] Alturaifi SA, Mathieu O, Petersen EL. Shock-tube laser absorption measurements of N2O time histories during ammonia oxidation. Fuel Communications. 2022 3;10:100050.

[26] da Rocha RC, Costa M, Bai XS. Chemical kinetic modelling of ammonia/hydrogen/air ignition, premixed flame propagation and NO emission. Fuel. 2019 6;246:24–33.

[27] Li Z, Li S. Effects of inter-stage mixing on the NOx emission of staged ammonia combustion. International Journal of Hydrogen Energy. 2022 1. Available from: https://doi.org/10.1016/j.ijhydene.2022.01.050.

[28] SUN Y, CAI T, SHAHSAVARI M, SUN D, SUN X, ZHAO D, et al. RANS simulations on combustion and emission characteristics of a premixed NH3/H2 swirling flame with reduced chemical kinetic model. Chinese Journal of Aeronautics. 2021 12;34(12):17–27.

[29] Khateeb AA, Guiberti TF, Zhu X, Younes M, Jamal A, Roberts WL. Stability limits and NO emissions of technically-premixed ammonia-hydrogen-nitrogen-air swirl flames. International Journal of Hydrogen Energy. 2020 8;45(41):22008–22018.

[30] Okafor EC, Somarathne KDKA, Hayakawa A, Kudo T, Kurata O, Iki N, et al. Towards the development of an efficient low-NOx ammonia combustor for a micro gas turbine. Proceedings of the Combustion Institute. 2019;37(4):4597–4606.

[31] European Commission DG Environment. Directive (EU) 2015/2193 of the European Parliament and of the Council of 25 November 2015 on the limitation of emissions of certain pollutants into the air from medium combustion plants (MCP Directive);.

[32] EPA. Air Pollution Control Technology Fact Sheet EPA-CICA Fact Sheet SCR 1. U.S. Environmental Protection Agency;.

[33] Shindell D, Bréon Fm, Collins W, Fuglestvedt J, Huang J, Koch D, et al. Anthropogenic and Natural Radiative Forc-ing. In: Climate Change 2013: The Physical Science Basis. Contribution of Working Group I; 2013.

[34] European Environment Agency. Greenhouse gas emission intensity of electricity generation by country; 2021. Available from: https://www.eea.europa.eu/data-and-maps/daviz/co2-emission-intensity-9/#tab-googlechartid_googlechartid_googlechartid_chart_1111.

[35] Versteeg HK, Malalasekera W. An Introduction to Computational Fluid Dynamics Second Edition. 2nd ed. Pearson; 2007. Available from: www.pearsoned.co.uk/versteeg.

[36] Baker C, Johnson T, Flynn D, Hemida H, Quinn A, Soper D, et al. Computational techniques. In: Train Aerodynamics: Fundamentals and Applications. Elsevier; 2019. p. 53–71.

[37] SIEMENS STAR-CCM+ documentation. Reynolds-Averaged Navier-Stokes (RANS) Turbulence Models;.

[38] Crowe CT, Schwarzkopf JD, Sommerfeld M, Tsuji Y. Multiphase Flows with Droplets and Particles. 2nd ed. CRC Press; 2011.

[39] SIEMENS STAR-CCM+ documentation. K-Epsilon Model;.

[40] Rodi W, Revell AJ, Benhamadouche S, Craft T, Laurencel' D, Yaqobi K. Engineering Turbulence Modelling and Experiments 6 A STRESS-STRAIN LAG EDDY VISCOSITY MODEL FOR UNSTEADY MEAN FLOW; 2005.

[41] Lardeau S, Billard F. Development of an elliptic-blending lag model for industrial applications. In: 54th AIAA Aerospace Sciences Meeting. vol. 0. American Institute of Aeronautics and Astronautics Inc, AIAA; 2016. .

[42] SIEMENS STAR-CCM+ documentation. Modeling Time;. Available from: file:///C:/Program%20Files/Siemens/16.04.012-R8/STAR-CCM+16.04.012-R8/doc/en/online/index.html#page/STARCCMP%2FGUID-1A72553E-917C-42AF-964B-C7B24B345AF5.html%23wwID0ETDOGB.

[43] Gas Phase Combustion—Flamelet Models;. Available from: https://docs.sw.siemens.com/documentation/external/PL20210401101005144/en-US/userManual/starccmp_userguide_html/index.html#page/STARCCMP%2FGUID-83013756-BBBE-4F7F-81B5-1C34D3023212.html%23.

[44] Cuenot B. Turbulent Combustion Modeling. vol. 95. Echekki T, Mastorakos E, editors. Dordrecht: Springer; 2011. Available from: www.springer.com/series/5980.

[45] Siemens. Flamelet Generated Manifold;. Available from: https://docs.sw.siemens.com/documentation/external/PL20210401101005144/en-US/userManual/starccmp_userguide_html/index.html#page/STARCCMP%2FGUID-EB53A2D4-3652-4F5C-A47F-CCE1AC340308.html%23.

[46] SIEMENS STAR-CCM+ documentation. Reacting Species Transport;.

[47] Stiehl B, Worbington T, Miegel A, Martin S, Velez C, Ahmed K. GT2019-91796 COMBUSTION AND EMISSION CHARACTERISTICS OF A LEAN AXIAL-STAGE COMBUSTOR. Phoenix; 2019.

[48] Stiehl B, Genova T, Otero M, Reyes J, Ahmed K, Martin S. Nox emission of an axial-staged combustor at high-pressure. In: AIAA Propulsion and Energy 2020 Forum. American Institute of Aeronautics and Astronautics Inc, AIAA; 2020. p. 1–10.

[49] Bösenhofer M, Wartha EM, Jordan C, Harasek M. The eddy dissipation concept-analysis of different fine structure treatments for classical combustion. Energies. 2018;11(7).

[50] Halouane Y, Dehbi A. CFD simulations of premixed hydrogen combustion using the Eddy Dissipation and the Turbulent Flame Closure models. International Journal of Hydrogen Energy. 2017 8;42(34):21990–22004.

[51] Goodwin DG, Speth RL, Moffat HK, Weber BW. Cantera: An Object-oriented Software Toolkit for Chemical Kinetics, Thermodynamics, and Transport Processes.; 2021. Available from: https://www.cantera.org.

[52] Fan Q, Liu X, Xu L, Subash AA, Brackmann C, Aldén M, et al. Experimental investigation of premixed ammonia combustion at high Karlovitz number conditions. Combustion and Flame. 2022.

[53] Baukal CE, Eleazer PB. Quantifying NOx for industrial combustion processes. Journal of the Air and Waste Management Association. 1998 1;48(1):52–58.

[54] Somarathne KDKA, Hatakeyama S, Hayakawa A, Kobayashi H. Numerical study of a low emission gas turbine like combustor for turbulent ammonia/air premixed swirl flames with a secondary air injection at high pressure. International Journal of Hydrogen Energy. 2017 11;42(44):27388–27399.

A

Model constants

The model constants applied to the lag EB $k - \varepsilon$ turbulence model and the EDC chemistry-turbulence interaction model are presented in Table A.1 and A.2, respectively.

Constant	Value
C_μ	0.22
C_T	1
C_t	4
σ_k	1
σ_ε	1.2
$C_{\varepsilon 1}$	1.44
$C^*_{\varepsilon 2}$	1.9
σ_φ	1

Table A.1: Lag k-ε model constants [37]

Constant	Value
C_{l1}	2.1377
C_{l2}	0.4082

Table A.2: EDC model constants [37]

B

Method development illustration

B.1 Convergence issues

Figure B.1 shows the mass fraction of N_2O at the outlet for a steady RANS simulation with applied clustering for chemistry acceleration, with a fuel mix of 30% cracked ammonia in the two main inlets and 42.8% cracked ammonia in the pilot and RPL. This figure illustrates the large oscillations obtained in some of the steady simulations, primarily caused by the clustering feature, as described in section 3.3.1. Note that the scale on of left axis is logarithmic.

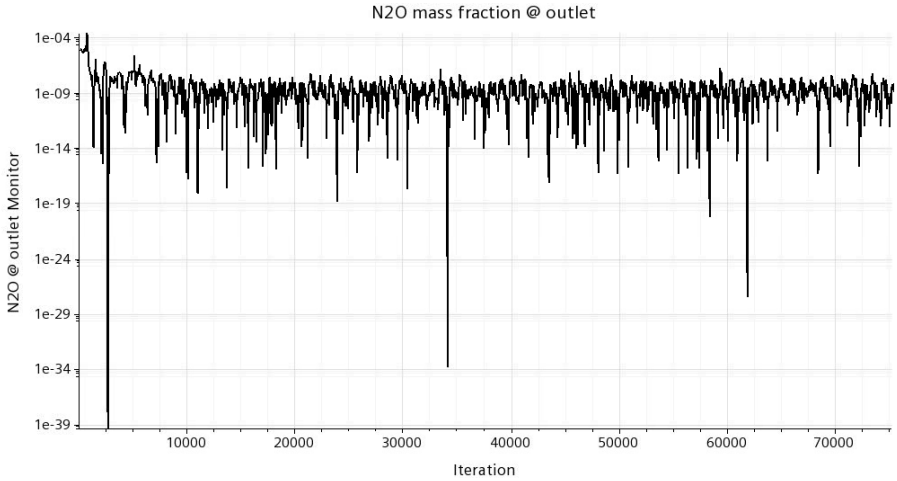

Figure B.1: N_2O mass fraction as a function of iterations for an steady RANS simulation

B.2 Time step size

Figure B.2 exemplifies the effect of time step size on the N_2O mass fraction at the burner outlet, as a function of number of iterations for an unsteady RANS simulation. There are three distinguishable regions with different trends in the N_2O mass fraction, which correspond to three different time step sizes:

1. Iteration 0 - 21 000: Δt= 1e-4 s
2. Iteration 21 000 - 31 200: Δt= 5e-5 s
3. Iteration 31 200 - 58 000: Δt= 5e-4 s

Due to the large effect of the time step size on the emissions, this method was not used further.

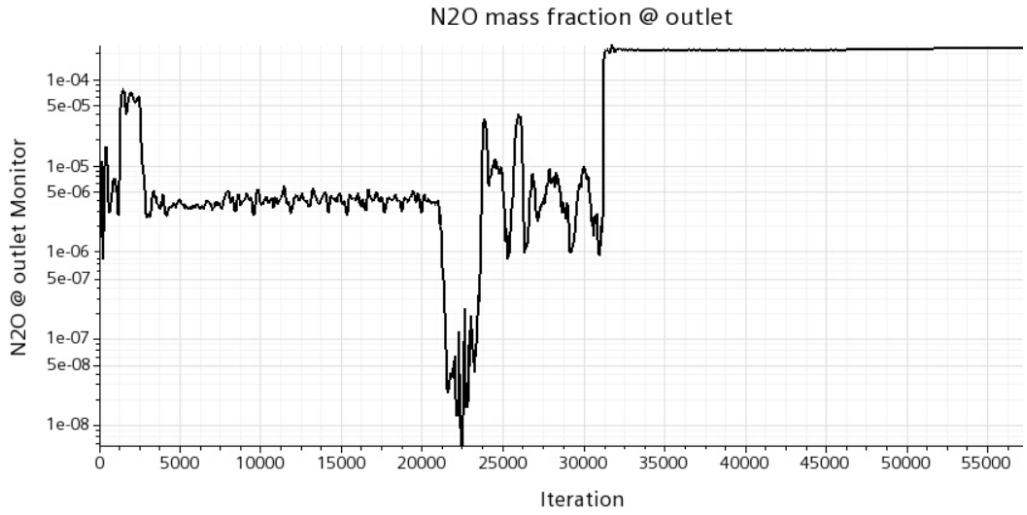

Figure B.2: N_2O mass fraction as a function of iterations for an unsteady RANS simulation, with varying time step size

B.3 Chemistry acceleration

Figure B.3 gives an example of how the monitored N_2O mass fraction is affected by the use of chemistry acceleration methods. Two different methods were applied; the clustering feature with default clustering parameters, and the in-situ adaptive tabulation (ISAT) method. The simulation was performed with a fuel composition consisting of 40% cracked ammonia in the two main inlets, and 42.8% cracked ammonia in the pilot and RPL. The two acceleration methods were compared to the non-accelerated case, and the results can be distinguished in figure B.3 by the following intervals:

1. Iteration 0 - 38 000: Clustering
2. Iteration 38 000 - 53 000: No acceleration
3. Iteration 53 000 - 75 000: ISAT with default settings

Due to the large effect of the acceleration methods on the results, none of the methods were used further.

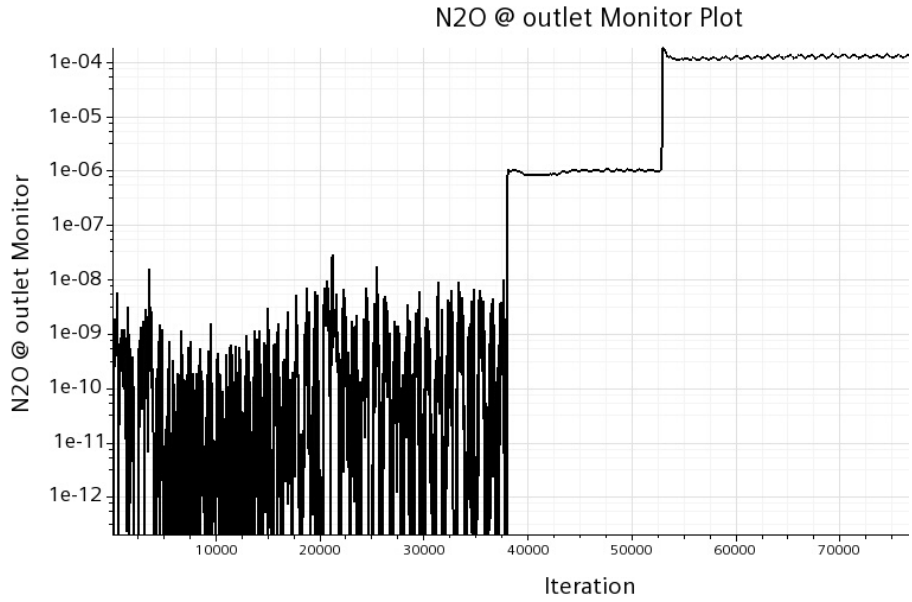

Figure B.3: N_2O mass fraction as a function of number of iterations for different chemistry acceleration methods

C

Auxiliary Cantera results

C.1 GWP in numbers

In this section the global warming potential (GWP) of the combustion process is presented in numbers. Table C.1 shows the GWP, in g CO_2-eq/kWh, of the CRN simulation without air staging, as a function of CD in the main channels. Table C.2 shows the GWP results of the air-staged CRN simulations. The results are shown for a range of ϕ_{PZ} (top row) and CD (leftmost column).

CD (main 1 & main 2)	GWP (g CO_2-eq/kWh)
0.0	433.7
0.01	427.4
0.1	376.2
0.2	325.0
0.3	276.6
0.4	231.7
0.5	188.5
0.6	147.7
0.7	108.5
0.8	72.1
0.9	37.6
0.99	8.8
1.0	6.0

Table C.1: Global warming potential in g CO_2-equivalents per kWh electricity, for non-staged combustion

CD / ϕ_{PZ}	0.5	0.6	0.7	0.8	0.9	1.0	1.1	1.2	1.3	1.4	1.5
0.0	315.9	98.2	41.3	19.0	9.2	5.6	13.2	54.1	169.2	337.0	512.5
0.01	296.9	107.9	44.1	17.9	8.7	5.3	12.3	53.8	168.9	337.7	486.1
0.1	245.6	83.5	32.9	14.6	7.6	4.6	8.7	33.0	111.4	259.5	415.7
0.2	188.8	60.5	26.0	12.2	5.8	3.8	6.1	19.6	73.7	176.1	322.5
0.3	143.3	50.0	20.3	9.3	4.8	3.2	4.74	11.7	42.4	118.6	235.6
0.4	106.7	35.4	15.6	7.1	4.0	2.7	3.6	7.2	23.0	73.4	159.7
0.5	77.4	27.9	10.8	5.4	3.2	2.4	3.0	4.8	12.8	39.0	98.7
0.6	54.2	18.8	8.0	4.4	2.7	2.1	2.5	3.4	6.8	19.9	54.3
0.7	35.6	12.1	5.8	3.3	2.3	2.0	2.2	2.6	4.0	9.4	25.8
0.8	21.0	8.0	4.0	2.6	2.0	1.8	2.0	2.2	2.7	4.5	10.8
0.9	9.6	4.1	2.6	2.0	1.8	1.7	1.8	1.9	2.1	2.5	3.8
0.99	2.1	1.8	1.8	1.8	1.7	1.7	1.7	1.8	1.8	1.9	1.9
1.0	1.8	1.8	1.8	1.7	1.7	1.7	1.7	1.8	1.8	1.8	1.8

Table C.2: Global warming potential in g CO_2-equivalents per kWh electricity, for air-staged combustion

C.2 Primary zone emissions

The emission of NO_X and N_2O from the primary zone (PZ) of the CRN model are shown in Figure C.1 and C.2 respectively. The emissions are given as a function of cracking degree, for different ϕ_{PZ}. No differences in NO_X emission levels between the primary and secondary zone for lean combustion (see Figure 4.2) can be observed. However, an increase in NO_X emission levels from the primary to the secondary zone is apparent for $\phi_{PZ} > 1$. If comparing Figure C.2 to Figure 4.3, the addition of secondary air affects the N_2O emissions remarkably.

The emissions from the primary zone of the 1D flame + PFR model are given in Figure C.3 and C.4, respectively. The trend and emission levels of NO_X for highly rich primary zones ($\phi_{PZ} \geq 1.4$) changes drastically with addition of secondary air (see Figure 4.5). This is likely a consequence of the large amount of unburned fuel exiting the primary zone at very rich conditions, enabling formation of fuel-NO_X in the oxygen-rich secondary zone. This effect is however not seen for N_2O.

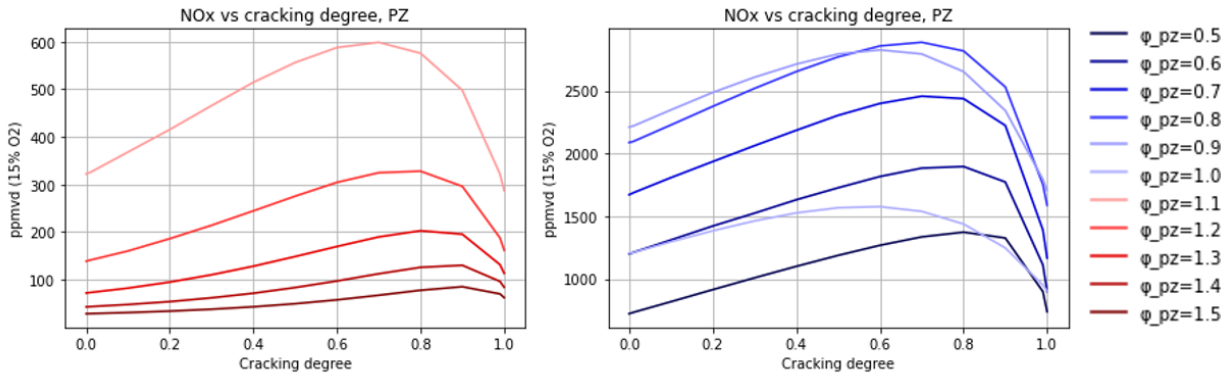

Figure C.1: NO_X emissions exiting the primary zone of the CRN, as a function of ϕ_{PZ} and CD

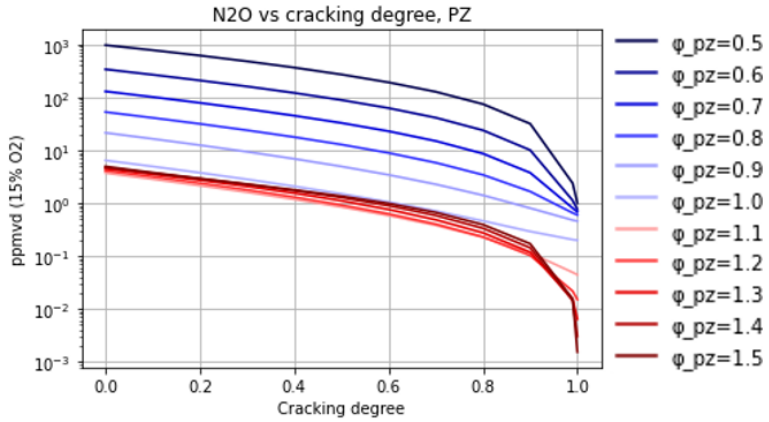

Figure C.2: N_2O emissions exiting the primary zone of the CRN, as a function of ϕ_{PZ} and CD

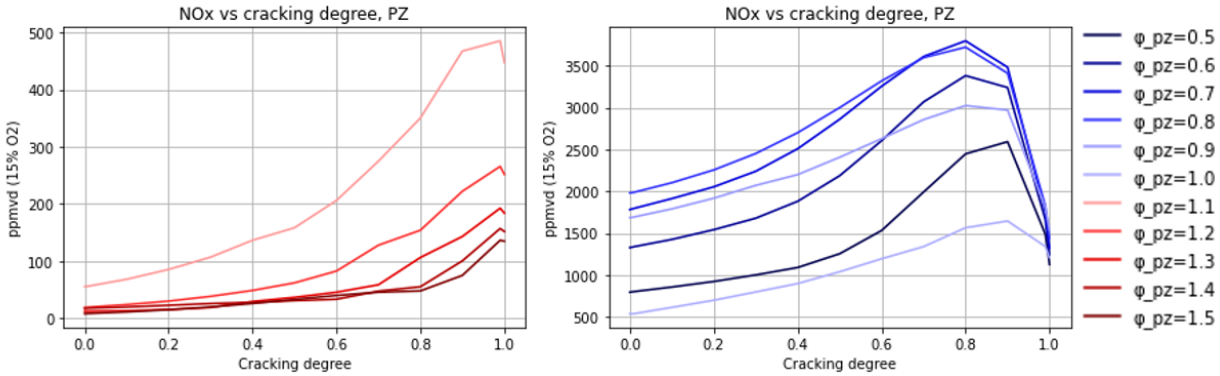

Figure C.3: NO_X emissions exiting the primary zone of the 1D flame + PFR model, as a function of ϕ_{PZ} and CD

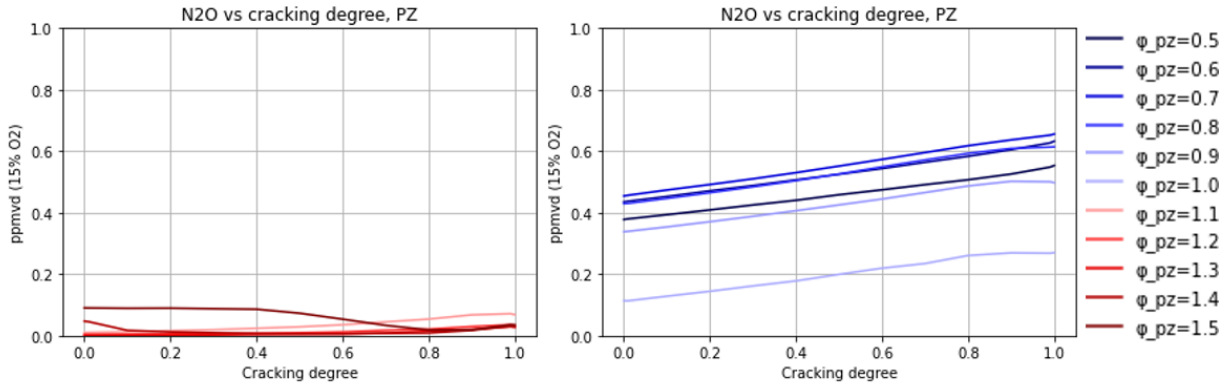

Figure C.4: N_2O emissions exiting the primary zone of the 1D flame + PFR model, as a function of ϕ_{PZ} and CD

C.3 Stagni mechanism

The chemical mechanism proposed by Stagni et al. [24] was applied to the two Cantera models. The resulting NO_X and N_2O emissions from single stage combustion are given in Figure C.5a and C.5b respectively. By applying the Stagni mechanism, the N_2O emissions of the CRN model are reduced by approximately 90% compared to the San Diego mechanism, Figure C.5a. In contrast, the N_2O emissions of the 1D flame model remain independent of the chemical mechanism. Smaller, but not insignificant, effects of mechanism on the NO_X emissions can be distinguished as well. Hence, an accurate chemical mechanism is of great importance to the quantitative analysis of ammonia combustion performance, and further experimental validation of the predicted emissions is needed.

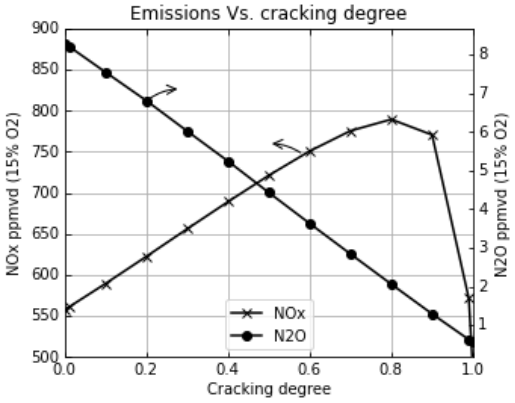

(a) CRN emissions

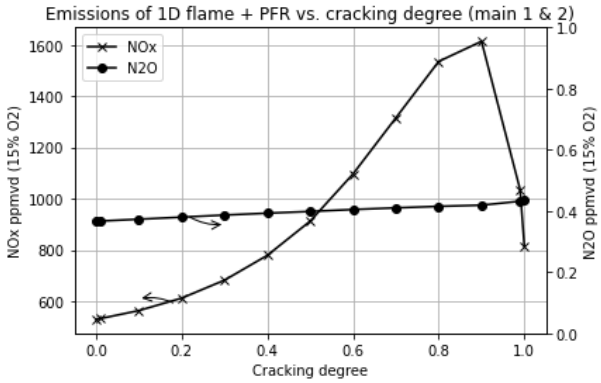

(b) 1D flame + PFR emissions

Figure C.5: NO_X and N_2O emissions as a function of ammonia cracking degree for lean combustion, with the Stagni mechanism

The NO_X and N_2O emissions from the CRN model under air-staged combustion are given in Figure C.6a and C.6b, respectively. If compared to the results of the San Diego mechanism, the NO_X levels are predicted similarly by both mechanisms. The N_2O levels are however approximately 90% lower than those of the San Diego mechanism. This once again points out the sensitivity of N_2O formation on the model parameters.

Finally, the Stagni mechanism was applied to the 1D flame + PFR model, and the resulting emissions are given in Figure C.7a and C.7b, respectively. The NO_X emission trends differ slightly from those of the San Diego mechanism, Figure 4.5, for high cracking degrees at $\phi_{PZ} > 1.0$. However, the 1D flame model produced similar results over all, for both mechanisms.

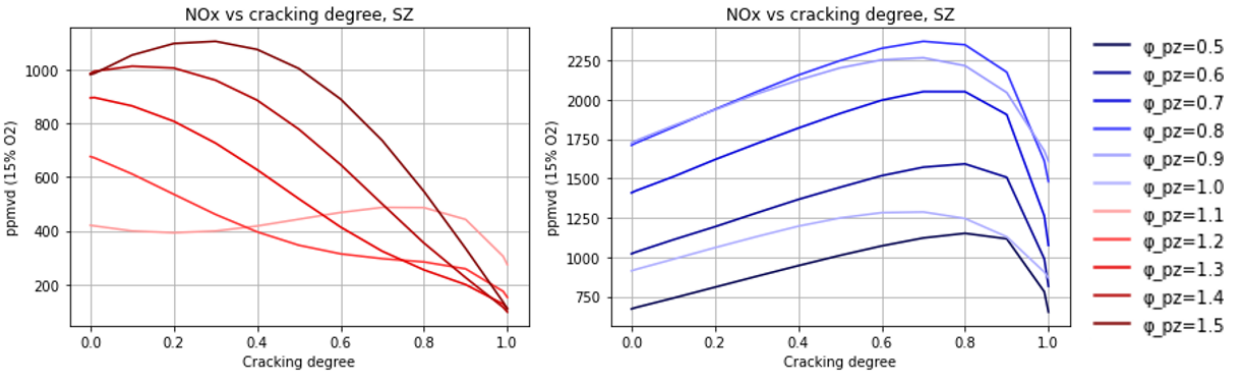

(a) NO_X emissions from rich combustion (red) and lean combustion (blue)

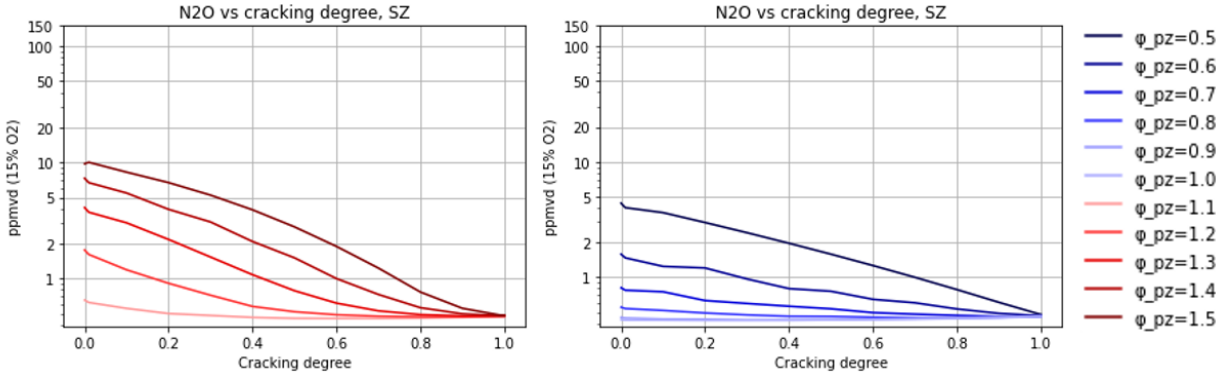

(b) N_2O emissions from rich combustion (red) and lean combustion (blue)

Figure C.6: Emissions from the CRN model as a function of cracking degree and equivalence ratio, with the Stagni mechanism

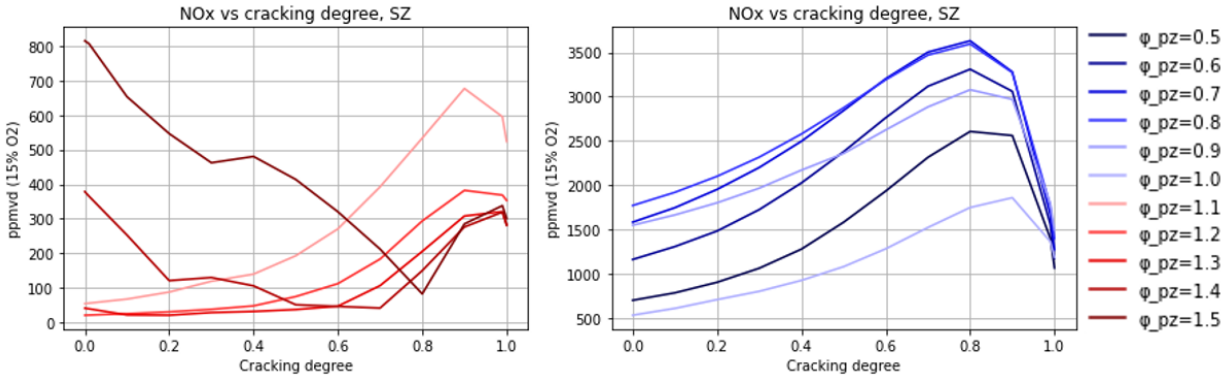

(a) NO_X emissions from rich combustion (red) and lean combustion (blue)

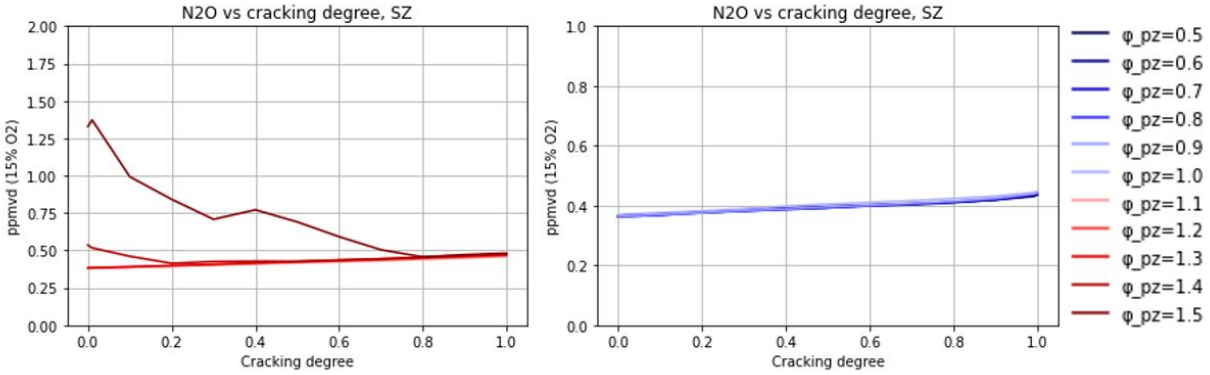

(b) N_2O emissions from rich combustion (red) and lean combustion (blue)

Figure C.7: Emissions from the 1D flame + PFR model as a function of cracking degree and equivalence ratio, with the Stagni mechanism

D

Flame properties of cracked ammonia

The laminar flame velocity (s_L) and normalized adiabatic flame temperature (T_{ad}) for single stage, lean combustion is shown in Figure D.1a and D.1b respectively, as a function of ammonia cracking degree. The adiabatic flame temperature is normalized to the combustor exit temperature. Since the laminar flame velocity is primarily used as a measure of predicting the risk of flashback and blow off, the four inlets (main 1, main 2, pilot and RPL) were simulated by separate 1D flames under lean conditions. Due to differences in equivalence ratio and fuel composition between the inlets, this could better indicate at which location the flame is exposed to a greater risk of flashback. Each inlet is therefore represented by a line in Figure D.1a and D.1b. For rich combustion, uniform cracking degrees and equivalence ratios were applied to all the inlets. Therefore, the flame properties of the rich combustion cases were simulated by a single flame.

The laminar flame velocity does not constitute an exact measure of the flame velocity under turbulent combustion, and thus the risk of flashback cannot be estimated quantitatively from the result in figure D.1a. However, s_L is directly correlated to the turbulent flame speed, and the result can be used for qualitative analysis. In Figure D.1a, the laminar flame velocities of the main channels increase rapidly with ammonia cracking degree, an expected result due to increasing H_2 content in the fuel. For the pilot gas mixture, s_L instead decreases with CD. This is due to the decreasing fuel-to air ratio, caused by a reduction in total fuel mass flow with increasing CD, see Table 4.2. s_L of the RPL is very low, independent of CD. To obtain a stable flame, the gas velocity should therefore be kept low in that region to avoid blow-off. Finally, the difference in s_L between the two main inlets is due to the first main inlet operating at a higher equivalence ratio compared to main 2.

Due to the fixed global flame temperature, T_{ad} of the main channels in Figure D.1b seems independent of CD. This does not indicate that the flame temperature is actually independent of CD, but rather that the flame temperature of the gas composition in the main channels must be constant to maintain the specified outlet temperature. There is, however, a notable decrease in T_{ad} for the pilot and RPL, with increasing CD. This is caused by the decrease in local fuel-to-air ratio, as described in the paragraph above. For CD > 0.9, no T_{ad} could be calculated for the RPL gas mixture. This is most likely due to the equivalence ratio being lower than the flammability limit of the given fuel compositions. Hence the lean combustor should not be operated at ammonia cracking degrees above 0.9, to avoid blow-out.

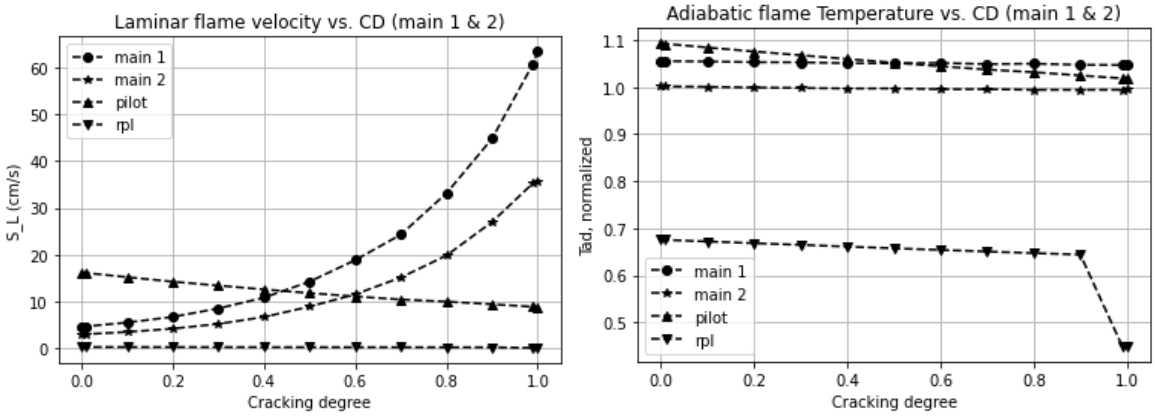

(a) Laminar flame velocity (cm/s) **(b)** Adiabatic flame temperature (K)

Figure D.1: Laminar flame velocity and normalized adiabatic flame temperature for the four different inlets as a function of CD (main 1 and main 2), without air staging

The laminar flame velocities and adiabatic flame temperatures as a function of cracking degree and equivalence ratio are shown in Figure D.2. Lean combustion cases are colored blue and rich combustion cases are colored red. Note that the y-scale is logarithmic, and that s_L increases exponentially with CD, as previously reported by R.C. da Rocha et al. among others [26]. Thus, combustion of ammonia at high CD is likely more prone to flashback. This is generally true also for increasing ϕ. However, s_L decreases with increasing ϕ at rich conditions, confirming the result of Y. Sun et al. [28] and Y. Jiang et al. [21].

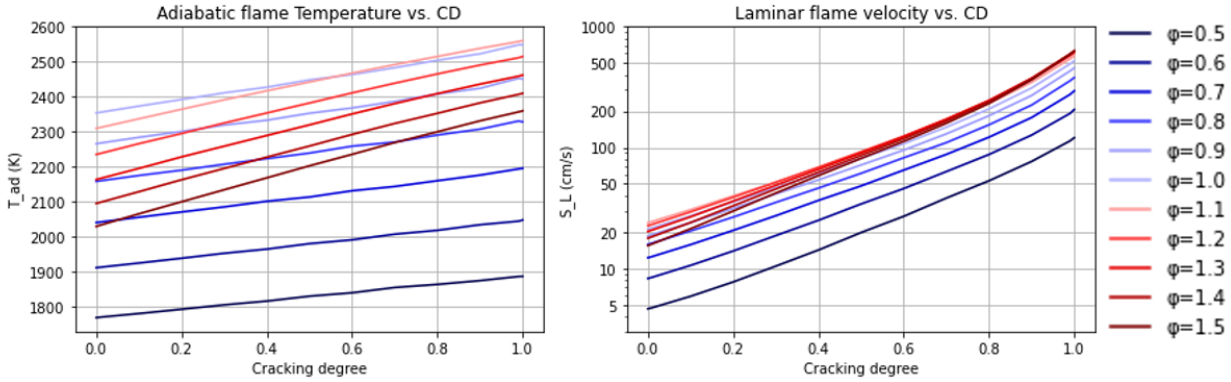

Figure D.2: Adiabatic flame temperature and laminar flame velocity of the primary zone for air-staged combustion, as a function of CD and ϕ.

The trend of adiabatic flame temperature with ϕ is similar to that of s_L. T_{ad} increases with ϕ for lean combustion, and decreases with ϕ for rich combustion. A maximum is reached close to stoichiometric conditions. At lean conditions, there is an increase in fuel-to-air ratio with ϕ, enabling a larger heat release per kg of gas mixture and a higher T_{ad}. In contrast, for $\phi > 1$, an increase in fuel-to-air ratio does not generate a larger heat release since oxygen is the limiting reactant. This causes the adiabatic flame temperature to drop in that range of ϕ.

E

Auxiliary CFD results

E.1 Rich CFD emissions

The emissions and total combustion efficiencies extracted from the primary zone of the rich combustion simulations in STAR-CCM+ are provided in Table E.1. The normalized temperature field of CD = 0.5 and $\phi_{PZ} = 1.2$ is given in Figure E.1. The flame is positioned close to the main inlets, indicating a risk of flashback.

CD (main 1 & 2)	$\phi_{main1+2}$	$\phi_{pilot+RPL}$	N_2O PZ (ppmvd)	NO_X PZ (ppmvd)	$\eta_{comb,tot}$
0.01	1.1	1.1	0.01	53.1	98.25%
0.01 (pilot + rpl 0.1)	1.1	1.1	0.01	55.9	98.32%
0.1	1.1	1.1	0.01	60.1	98.16%
0.1	0.5	1.1	0.403	916.4	99.997%
0.2	1.1	1.1	0.02	75.0	98.06%
0.3	1.1	1.1	0.02	83.0	97.87%
0.5	1.2	1.2	0.004	21.8	93.9%

Table E.1: Emissions and total combustion efficiency from the rich CFD simulations

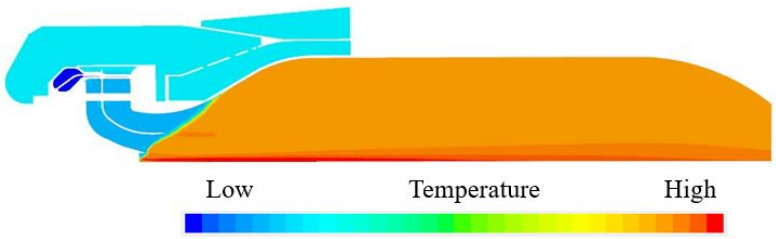

Figure E.1: Normalized temperature field of 50% cracked ammonia, at $\phi_{PZ} = 1.2$

DEPARTMENT OF SOME SUBJECT OR TECHNOLOGY
CHALMERS UNIVERSITY OF TECHNOLOGY
Gothenburg, Sweden
www.chalmers.se

CHALMERS
UNIVERSITY OF TECHNOLOGY